



Research Article

Smart Aggregate-Based Concrete Stress Monitoring via 1D CNN Deep Learning of Raw Impedance Signals

Quoc-Bao Ta ¹, Quang-Quang Pham,¹ Ngoc-Lan Pham,¹ Thanh-Canh Huynh ^{2,3}, and Jeong-Tae Kim ¹

¹Department of Ocean Engineering, Pukyong National University, 45 Yongso-ro, Nam-gu, Busan 48513, Republic of Korea

²Faculty of Civil Engineering, Duy Tan University, Da Nang 550000, Vietnam

³Institute of Research and Development, Duy Tan University, Da Nang 550000, Vietnam

Correspondence should be addressed to Jeong-Tae Kim; idis@pknu.ac.kr

Received 15 August 2023; Revised 17 January 2024; Accepted 27 February 2024; Published 9 March 2024

Academic Editor: Young-Jin Cha

Copyright © 2024 Quoc-Bao Ta et al. This is an open access article distributed under the Creative Commons Attribution License, which permits unrestricted use, distribution, and reproduction in any medium, provided the original work is properly cited.

A 1-dimensional convolutional neural network (1D CNN) model is developed to process deep learning of raw impedance signals for smart aggregate (SA)-based concrete stress monitoring. First, the framework of the SA-based stress monitoring using deep learning of raw impedance signals is described. An impedance measurement model is designed for a SA-embedded concrete body under compression. A 1D CNN model is developed for deep learning of raw impedance signals corresponding to various stress levels. Three approaches for concrete stress monitoring are designed to deal with data availability, signal noises, and untrained stress levels. Second, a few SA-embedded concrete cylinders are experimented to measure impedance signals under various stress levels. Finally, the performance of the proposed method is extensively evaluated by investigating the feasibility of the K-fold cross-validation to deal with the data availability and the effects of signal noises and untrained data on the accuracy of stress estimation in the SA-embedded concrete cylinders.

1. Introduction

Concrete structures play an irreplaceable role in construction due to their flexibility and cost-effectiveness. During the long service life, damage or degradation can be occurred in critical members under continuous compression. To prevent the local damage-induced catastrophic failure of the concrete structure, a continuous stress-monitoring task should be applied as a prerequisite procedure [1–3].

Various nondestructive testing methods are available for structural health monitoring (SHM) of concrete structures. They include X-ray scan [4, 5], fiber-optic sensor [6], piezoelectric sensor [7], and cement-based sensor [8]. Among those, strain-based methods are commonly used to monitor concrete stress. External strain sensors (e.g., electrical strain gauges and vibrating wires) can be attached to concrete surfaces to accurately measure axial strains [9, 10]. The sensitivity of the external strain sensor is insufficient for detecting the occurrence of concrete cracks. A few

researchers have attempted to monitor the concrete stress using embedded strain gauges [11] and fiber Bragg grating (FBG) sensors [12].

In demand for real-time SHM, the electromechanical impedance (EMI) technique has gained attention due to its advantages in sensing and driving functionalities, fast response speed, stable performance, and low cost [13]. This technique utilizes the coupling interaction between a PZT (lead zirconated titanate) transducer and the monitored structure to provide information about the local structural characteristics of the examined region [14]. Previous studies used PZT sensors placed on the surface of concrete structures to detect changes in EMI signals induced by local damage near the concrete surface [15].

The surface-mounted PZT sensor is less sensitive to inner concrete damage positioned away from the surface [7]. As an emerging alternative for concrete damage monitoring, Song et al. [16] proposed a smart aggregate (SA) technique. The SA-based damage monitoring has shown promising

capabilities in detecting early signs of concrete damage [17]. The change of concrete stress and the occurrence of damage can directly affect the variation of the EMI signal acquired from the SA sensor. In addition, the effects of noisy ambient conditions and temperature variations on the EMI signals could be reduced by adopting the SA sensor as compared to that of the surface-bonded PZT sensor.

As compared to the FBG sensing technique, the EMI technique is more cost-effective, with noninstructive installation and a larger area coverage [18]. The EMI technique utilizes cheap PZT sensors and low-cost measurement devices [19, 20], while FBG sensors and associated measurement devices used in the FBG sensing technique are more expensive [12, 21]. For SHM of concrete structures, the SA serves a dual role as an aggregate and sensor, facilitating convenient installation, while the physical installation of FBG sensors can be more challenging and may disturb the concrete during placement. Moreover, the PZT sensor used in the EMI technique can cover relatively larger sensing areas [22], while the FBG sensor only records the point's response, thus requiring more sensors for comprehensive monitoring of large structures [23]. Nevertheless, the EMI technique has some drawbacks [18], including the susceptibility of the PZT sensors to environmental conditions such as temperature and humidity, along with the need for specialized knowledge in data interpretation and meaningful feature extraction [24, 25].

An important issue of the SA-based monitoring is to deal with multisteps of data gathering, information processing, and decision making. Traditional multisteps could have the difficulty in quantitative stress evaluation and result in false damage alarms due to the biased selection of EMI features, the lack of expertized analysis, and the human-interfered wrong decision. The EMI features such as root-mean-square deviation (RMSD) and cross-correlation deviation (CCD) are commonly used to quantify the changes in EMI signals for stress estimation and damage detection [7, 17, 26, 27]. However, the selection of suitable frequency bands and meaningful EMI features turns out a challenge that costs the accuracy of evaluation results [28, 29]. In addition, the hand-crafted feature extraction may limit the existing technique from a real-time operation. Therefore, there is a need to develop an alternative method for stress monitoring with automated EMI feature extraction.

In recent years, convolutional neural network (CNN)-based deep learning algorithms have been effectively adopted to estimate the structural conditions of civil infrastructures [30–37]. Traditional damage detection methods often consist of two steps which are “feature extraction” and “damage identification” [30]; meanwhile, CNN-based methods execute these steps in a unified procedure [31]. The CNN can directly process raw signals and autonomously learn optimal features for damage identification, considerably reducing the initial processing workload [31]. A few researchers have examined the combination of the CNN algorithms with the EMI-based technique for damage assessment. Na et al. [32] proposed an artificial neural network model which learns EMI signals to detect bolt loosening in a steel-bolted joint. The proposed method

achieved high accuracy even with a small number of training EMI data. De Oliveira et al. [33] used PZT sensors and a CNN-based deep learning algorithm to accurately detect damage in an aluminum plate. Nguyen et al. [34] presented a 1D CNN model to autonomously process the raw EMI response for transducer failure detection. Recently, Nguyen et al. [37] have developed a 1D CNN model for EMI-based bolt-loosening monitoring and assessment in steel structures without any data preprocessing.

To date, a few research efforts have been made to integrate the CNN algorithms with the EMI technique for health monitoring of concrete structures [38–43]. The performance of the 1D CNN algorithm for autonomous damage-sensitive feature learning of EMI responses was evaluated for damage monitoring of a prestressed reinforced concrete girder [35]. To overcome the shortcomings of the EMI-based stress and damage quantification, Ai et al. [38] proposed a simple 2D CNN to identify compressive stress and load-induced cracking damages in a concrete cubic structure. In a later study, Ai and Cheng [39] split the EMI signatures into subrange responses and processed them by a statistical approach to construct the 2D input for training and testing the deep learning model. Their experimental results showed that the proposed 2D CNN model was of high accuracy even to minor damages. Recently, Ai et al. [40] proposed a 1D CNN approach for exploiting the raw admittance response to automatically detect small-size damages in concrete structures. The comparison with a traditional back propagation neural network showed significant superiority of the proposed 1D CNN model in terms of prediction accuracy. Also, Li et al. [44] integrated the EMI technique with a CNN-based regression model for quantitatively predicting and monitoring the real-time concrete strength development. Yan et al. [42] developed an EMI-integrated 1D CNN feature extraction network for monitoring early-age hydration of cement mortar. The proposed approach could quantitatively evaluate dynamic penetration impedance with high accuracy, outperforming traditional machine learning methods. Zhang et al. [43] applied 2D CNN for assessing concrete-rock interface debonding via PZT-based ultrasonic measurement. The proposed model could predict delamination damage in concrete-rock interface with high accuracy, even with different concrete interfacial roughness. These studies have demonstrated the applicability of CNN models as an effective means for stress monitoring and damage identification in concrete infrastructures.

Despite those research efforts, there are at least three remaining issues. (1) The previous studies have mostly focused on developing the CNN models for processing the EMI data obtained from the surface-mounted PZT sensor [38–41], which is less sensitive to inner structural changes [7]. (2) The previous PZT-embedded SA techniques mostly rely on manually extracting EMI features from specific frequency bands that could limit the effectiveness of these techniques regarding the accuracy and computational cost. (3) The generalization capability of the CNN approach to deal with data availability, signal noises, and untrained stress levels for concrete stress estimation still lacks of

investigation. To address these issues, this paper proposes a combined scheme of the 1D CNN deep regression learning model and the SA-based EMI measurement technique for concrete stress monitoring as an attempt to realize an autonomous SHM in concrete structures.

The major contributions of this work lie in the following: (1) the proposed method develops an efficient 1D CNN approach for smart aggregate (SA)-based concrete stress monitoring to autonomously process deep regression learning of raw EMI signals. (2) The method can significantly reduce the signal processing costs related to manual data transformation and damage-sensitive feature extraction for the SA-based EMI technique. (3) A few approaches for concrete stress monitoring, including deep learning of K-fold cross-validation and deep learning of noise-contaminated databank and partially-untrained databank, are designed and sufficiently validated in experiments to demonstrate the robustness and the generalization of the proposed 1D CNN model.

The remaining parts of the paper are organized as follows. The research framework, the SA-based EMI measurement technique, the architecture of the proposed 1D CNN regression model, and three concrete stress monitoring approaches are explained in the second section. The next one presents experiments on SA-embedded concrete specimens and statistical quantification of EMI features. In the fourth section, the validation of the proposed method is presented via predicting the compressive concrete stress in the tested concrete specimens. In the last section, concluding remarks are drawn.

2. Methodology

2.1. Research Framework. The conventional approach for stress monitoring using a PZT-embedded SA technique relies on manually extracting EMI features from specific frequency bands. This process is time consuming and requires trial and error in selecting the frequency bands for reliable results [29]. Furthermore, a hand-crafted EMI feature extraction hinders the real-time operation of existing techniques [45]. Hence, an alternative approach for automated raw EMI feature extraction using deep learning needs to be sought.

Figure 1 illustrates a research framework for SA-based concrete stress monitoring via a 1D CNN deep learning of raw EMI signals. The proposed framework consists of the following three main phases: (1) EMI data acquisition via the SA technique, (2) development of 1D CNN deep learning model, and (3) approaches for concrete stress monitoring. In phase 1, a series of raw EMI signals and their corresponding structural properties (such as stress levels or damage severities) are acquired to build datasets for stress monitoring in SA-embedded concrete cylinders. In phase 2, the 1D CNN deep learning model is developed for autonomous processing and feature extraction of raw EMI signals. The proposed model can be trained on a massive amount of EMI signals and their corresponding stress levels to return the output for evaluating and predicting concrete stress.

In phase 3, three stress monitoring approaches are implemented for the SA-embedded concrete cylinders, from which EMI signals are measured for a series of compressive loadings. The first approach is to estimate the stress magnitudes from deep learning of an available databank via K-fold cross-validation. The second approach is to predict the stress magnitudes from deep learning of a noise-contaminated databank. The third approach is to predict the stress magnitudes from deep learning of a partially-untrained databank. These three approaches are utilized to evaluate the performance of the developed model (i.e., 1D CNN deep learning model) on the limited databank built from the measured EMI datasets.

2.2. SA-Based EMI Technique. A model of SA-based EMI monitoring for concrete structures is illustrated in Figure 2. A protected PZT sensor is embedded into a small concrete block to fabricate the SA. During concrete casting, the SA is placed within an inspected structure to acquire raw EMI signatures via the interaction between the PZT-embedded SA and the monitored structure (see Figure 2(a)). Note that the structural characteristics of the protected glue layer (e.g., epoxy), the small concrete sample, and the target structure would be changed corresponding to the variation of the applied force N .

A 3 degrees of freedom (3-DOF) EMI model [7, 46] is used to demonstrate the coupling motions of the coated layer, the concrete block, and the monitored structure (see Figure 2(b)). The coupled structural-mechanical impedance Z_c of the host structure, concrete SA member, and the protective glue layer can be presented as follows [7, 46]:

$$Z_c = \frac{1}{j\omega} \left(T_{11} - \frac{T_{12}^2}{T_{11} + (T_{22} - T_{23}^2/T_{33})} \right), \quad (1)$$

where the dynamic stiffness parts, T_{ab} ($a, b = 1 - 3$), depend on the structural features of the protective glue layer, concrete SA member, and investigated host structure [7, 46].

The EMI $Z(\omega)$ is a function of the structural-mechanical impedance of the PZT sensor and that of the SA-host structure [14]:

$$Z(\omega) = \left\{ j\omega \frac{w_{pzt} l_{pzt}}{t_{pzt}} \left[\hat{\epsilon}_{33}^T - \frac{1}{Z_{pzt}(\omega)/Z_c(\omega) + 1} d_{31}^2 \hat{Y}_{11}^E \right] \right\}^{-1}, \quad (2)$$

where the parameters w_{pzt} , t_{pzt} , and l_{pzt} represent the width, thickness, and length of the piezoelectric patch, respectively; $\hat{\epsilon}_{33}^T$ denotes the complex dielectric constant at zero stress; $Z_{pzt}(\omega) = \hat{Y}_{11}^E w_{pzt} t_{pzt} / j\omega l_{pzt}$ is the structural-mechanical impedance of the PZT patch; d_{31} denotes the constant of the PZT sensor in one direction at zero stress; and \hat{Y}_{11}^E signifies the intricate Young's modulus of the PZT plate under the zero electric field condition.

As shown in equation (2), the real part of impedance $Z(\omega)$ contains the SM impedance of the PZT patch ($Z_{pzt}(\omega)$) and of the SA-host structure ($Z_c(\omega)$). Since PZT patch keeps

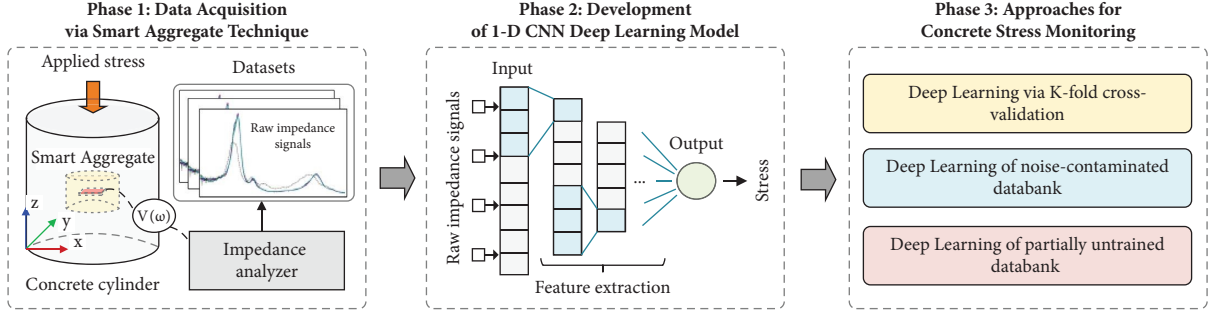


FIGURE 1: Research framework for the SA-based concrete stress monitoring method via 1D CNN deep learning of raw EMI signals.

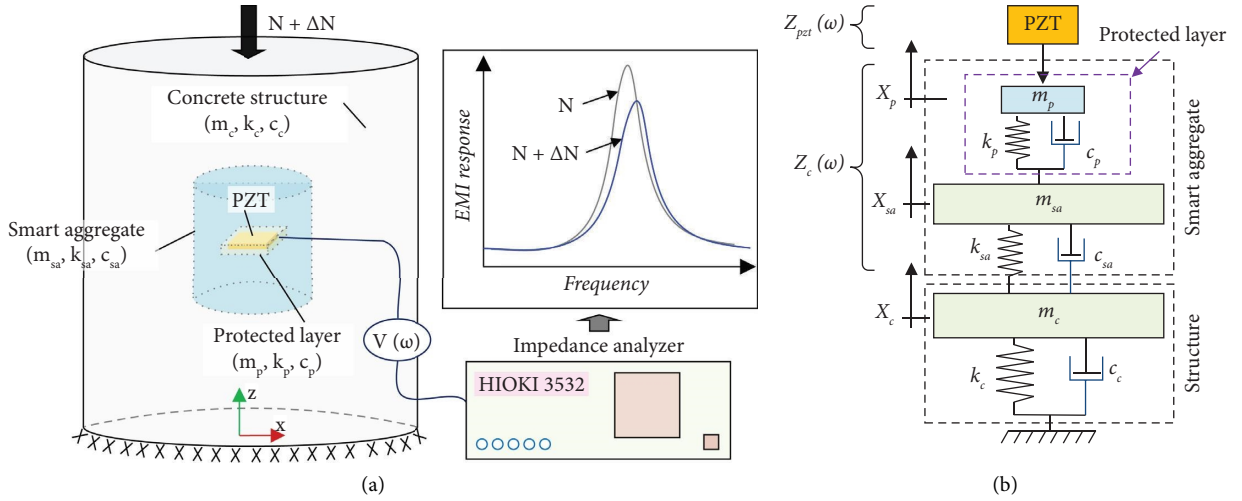


FIGURE 2: SA-based EMI measurement model for concrete structure. (a) SA-embedded concrete structure. (b) 3-DOF model.

constant in mechanical and electrical characteristics, any structural changes (e.g., stress variation or structural damage) can be directly reflected to changes in the measured EMI signatures. The unique advantage of the SA-based EMI technique is that the SA can give a fixed resonant EMI band regardless of the host structure, thereby enhancing its adaptability to monitor other stress types such as tension and shear and other concrete types and mixture proportions.

2.3. 1D CNN Model. To enable autonomous damage feature learning and concrete stress prediction, a 1D CNN-based regression model is developed for stress monitoring in SA-embedded concrete structures. The architecture of the proposed 1D CNN was developed based on the previous well-established model [47], and the hyperparameters were tuned using the practical guidance in [48]. To select an appropriate architecture for the 1D CNN model, a preliminary study has been conducted, as presented in Appendix A. Four 1D CNN architectures (M1–M4) with different depths are designed, and their performances are compared. According to the comparison results, the best architecture (M2) is selected for concrete stress monitoring and depicted in Figure 3.

The selected 1D CNN architecture consists of the following three main parts: input, hidden layers, and output. The 1D CNN deep learning model receives $N \times 501$ input

data, where N represents the number of raw EMI signals, and each signal has 501 measurement points within its frequency bands. More information about the raw EMI signals can be found in Section 3.3. The model then generates an output for evaluating and predicting concrete stress. The hidden layers include four convolutional (Conv) layers, four rectified linear unit (ReLU) layers, four max pooling (Maxpool) layers, three fully-connected (Fc) layers, and a regression output (Regression) layer.

The specifications of the 1D CNN layers are outlined in Table 1. The Conv layer consists of trainable filters or kernels. Each filter generates a frame of the feature map in the subsequent subsampling layer. The depth of the convolution layer is equal to the number of frames. The ReLU layer converts negative values from the output of the preceding layer to zero while keeping all positive values. The Maxpool layer slides filters over the output of the preceding layer and extracts the element with the highest value. The function of the Maxpool layer is to reduce the computational cost by reducing the size of the feature map. The Fc layers connect all possible connections layer to layer, meaning every input from the preceding layer influences every element of the output layer. The Fc layers combine and transform learned features into lower-dimensional representations suitable for the regression layer. The regression layer is responsible for regressing the stress value. It computes the loss value via

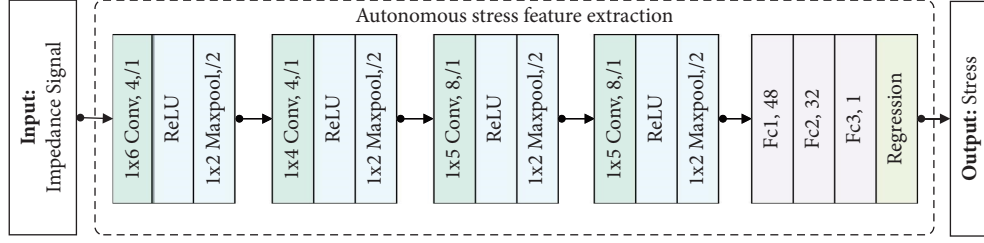


FIGURE 3: Architecture of the 1D CNN deep learning model using SA's raw EMI signals.

a mean absolute error (MAE) metric. A root mean square error (RMSE) metric is also calculated to provide further information about the model's accuracy.

Loss and RMSE values are quantified by equations (3) and (4). The symbol n denotes the number of signals. y_i and \hat{y}_i (unit in MPa) represent the predicted stress and the actual stress, respectively, for the i^{th} signal. Loss value is measured as the average value of absolute differences between predicted and actual stress. RMSE is calculated as the average of the squared difference between predictions and actual stress. Loss and RMSE values indicate the stress prediction error in terms of stress monitoring with a unit in MPa.

$$\text{Loss} = \frac{1}{n} \sum_{i=1}^n |y_i - \hat{y}_i|, \quad (3)$$

$$\text{RMSE} = \sqrt{\frac{1}{n} \sum_{i=1}^n (y_i - \hat{y}_i)^2}. \quad (4)$$

2.4. Stress Monitoring Approaches

2.4.1. Deep Learning via K-Fold Cross-Validation. The performance of a deep learning model depends on the data availability, and most deep learning models lack accuracy when they are trained using unbalanced datasets [49]. To address this issue, this study adopted a specific K-fold cross-validation technique called stratified shuffle split [50]. The schematic of K-fold cross-validation is illustrated in Figure 4. Total 10 folds were created from the datasets of the measured raw EMI signals. In each fold, the raw EMI signals were randomly divided into a training fold (75% of the data) and an evaluation fold (25% of the data). The performance of each fold in the K-fold cross-validation process was evaluated, and the averaged performance (E) was used to represent the overall performance of the K-folds.

Figure 5 illustrates the schematic of a 1D CNN deep learning approach using K-fold cross-validation. It consists of the following two parts: "data acquisition and preparation" and "1D CNN training and evaluation". In the first part, a set of raw EMI signals and their corresponding structural properties (e.g., stress levels or damage severities) are acquired to form datasets for deep learning. Then, the K-fold cross-validation is employed to classify the collected datasets into training and evaluation fold datasets. In the second part, a series of deep learning stages are performed to

TABLE 1: Specifications of 1D CNN layers.

Nos.	Type	Depth	Filter	Stride
1	Conv	4	1×6	1
2	ReLU	—	—	—
3	Maxpool	—	1×2	2
4	Conv	4	1×4	1
5	ReLU	—	—	—
6	Maxpool	—	1×2	2
7	Conv	8	1×5	1
8	ReLU	—	—	—
9	Maxpool	—	1×2	2
10	Conv	8	1×5	1
11	ReLU	—	—	—
12	Maxpool	—	1×2	2
13	Fc ₁	48	—	—
14	Fc ₂	32	—	—
15	Fc ₃	1	—	—
16	Regression	—	—	—

identify the 1D CNN deep learning model (so-called 1D regression model). The training fold datasets (i.e., EMI datasets and their corresponding stress levels) are utilized for deep learning of the 1D CNN model. The evaluation fold datasets are employed to assess the performance of the trained model on unseen data. In brief, the performance of the 10-fold cross-validation technique on the model's generalization capability is investigated for the available raw EMI datasets (as presented in Section 4.1).

2.4.2. Deep Learning of Noise-Contaminated Databank. EMI signals can be affected by various factors, such as sensor geometry and temperature [48, 51]. Conducting experiments that consider all of these factors can be challenging and costly. Therefore, data argumentation is a feasible alternative to considering the realistic measurement conditions of the investigated structure. One common way of data argumentation is the addition of Gaussian noise [52] to the measured EMI signals. The Gaussian noise has two parameters, mean zero and standard deviation. By adjusting the standard deviation value, the measured signal will be injected at different noise levels. The formula for noise injection can be expressed as follows:

$$x[n] = s[n] + w[n] \times s[n], \quad (5)$$

where $x[n]$ is the noise-contaminated EMI signal, $s[n]$ is the measured EMI signal, $w[n]$ is the Gaussian noise, and n is the number of investigated measurement points. The effect

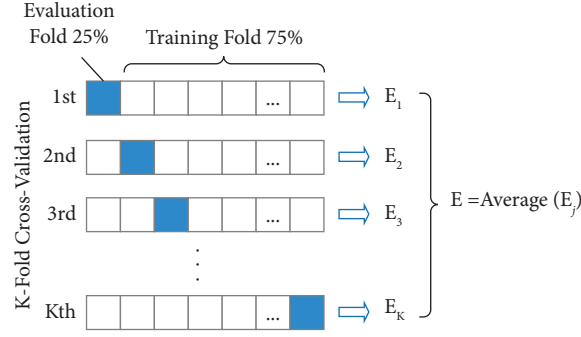


FIGURE 4: Data preparation via K-fold cross-validation.

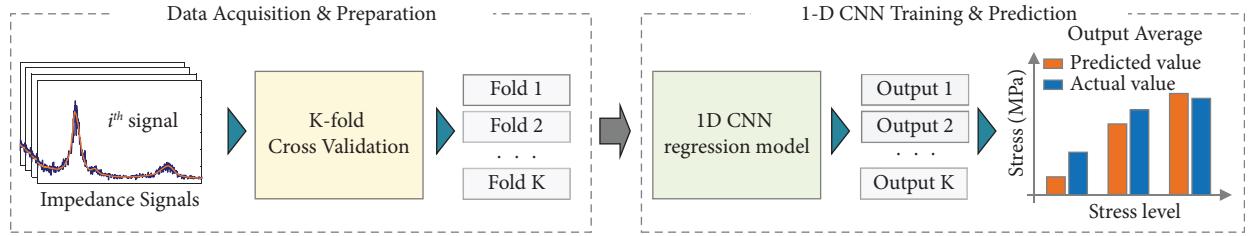


FIGURE 5: Schematic of deep learning via K-fold cross-validation.

of noise-contaminated databank on the robustness of the 1D CNN deep learning model is investigated for a variety of noise levels (as presented in Section 4.2).

2.4.3. Deep Learning of Partially-Untrained Databank. Deep learning techniques often lack robustness and generalizability when trained with limited data [53]. A high-performing deep learning model is one that can learn from a smaller amount of data. In this study, we reduce the number of training data in the databank to evaluate the performance of the 1D CNN deep learning model for predicting untrained stress levels with nonlinearities characteristics of raw EMI responses [28]. In brief, the effect of a partially-untrained databank on the robustness and generalization of the 1D CNN deep learning model is investigated for untrained concrete stress levels (as presented in Section 4.3).

3. Experimental Test

3.1. SA Fabrication. The SA was fabricated as shown in Figure 6. The PZT 5A patch ($10 \times 10 \times 1$ mm) was joined with electric wires to form a PZT sensor for EMI measuring. The sensor was protected by an epoxy layer of around 0.5 mm thickness (see Figure 6(a)). A PVC mold (height 26 mm and inner diameter of 26 mm) was used for concrete casting (see Figure 6(b)). The coated PZT sensor was embedded in the center of the mold to form a SA sensor (see Figure 6(c)). As the light-weight concrete, the mixture of SA consists of cement, sand, and water (see Table 2). After 48 hours of casting, the SA was removed from the mold and moisture cured for 28 days. The SA samples are shown in Figure 6(d). The material properties of the components for the SA are listed in Table 3.

3.2. SA-Embedded Concrete Cylinder. Figure 7 presents a fabrication procedure of SA-embedded concrete cylinder. The SA sensor was positioned centrally within the cylindrical mold sized 100×200 mm. As shown in Figure 7(a), we utilized aluminum plates, plastic wires, and a thin steel bar to position the SA sensor at the center of the cylinder. As a positioning interface, the aluminum plate with a center hole (ϕ 1 mm) was connected to a thin plastic wire (ϕ 0.5 mm) hanging about 100 mm. The electric wires were connected to the SA sensor via the side surface of the mold (drilled with a small hole around ϕ 3 mm). A super glue (Loctite 401) was used to mount the aluminum plate onto the SA's surface and to place the aluminum plate at the bottom surface of the cylindrical mold.

Figure 7(b) shows the casting process of the SA-embedded concrete cylinder. The concrete mixture was selected as listed in Table 2. Concrete cylinders were cured using wet blankets for 28 days. Three SA-embedded concrete cylinders were fabricated for EMI monitoring. The SA 1–3 sensors were installed in the concrete cylinders 1–3, respectively. These sensors were fabricated by using the same concrete mixture as listed in Table 2 and constructed at the same time.

3.3. Experimental Setup. Figure 8 shows the test setup of the concrete cylinders (i.e., cylinders 1–3 embedded with SAs 1–3) under compression forces. As shown in the figure, the concrete samples were placed inside a load frame of a servohydraulic materials test system (MTS system). The real compression force was monitored by a load cell with a capacity of 500 kN. The measurement of EMI signals from the SA sensors was conducted via an impedance analyzer,

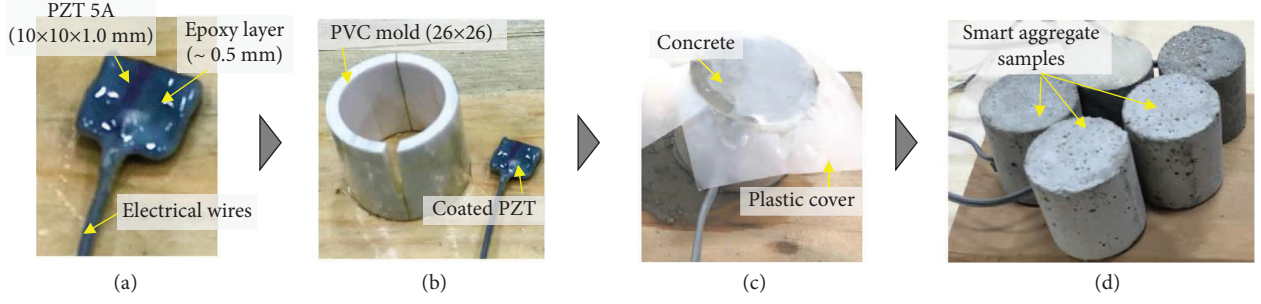


FIGURE 6: Fabrication of SAs. (a) Coated PZT. (b) PVC mold. (c) Concrete casting. (d) SAs.

TABLE 2: Concrete mixture for SA sensor*.

Material for 1 m ³	Mass (kg)
Sand	710
Coarse aggregate (D_{\max} 25)**	948
Cement	425
Water (liter)	170

*Concrete mixture was used for concrete cylinder specimens in next section; **SA sensor was constructed without coarse aggregate.

TABLE 3: Material properties of components for SA sensor.

Properties	PZT 5A	Epoxy layer	Concrete
Mass density, ρ (kg/m ³)	7750	1090	2400
Young's modulus, E (GPa)	62.1	0.75	25.43
Poisson's ratio, ν	0.35	0.3	0.2
Compressive strength, σ_c (MPa)		32.3	25.3*
Damping loss factor, η	0.0125		
Dielectric constant, ϵ_{33}^T (F/m)	1.53×10^{-8}		
Coupling constant, d_{31} (m/V)	-1.71×10^{-10}		
Dielectric loss factor, δ	0.015		

*Compressive strength was determined by a uniaxial compressive test on three standard concrete cylinders (100 × 200 mm).

HIOKI 3532. The room temperature was also monitored via Kyowa EDX-100A during the experiment.

Figure 9 shows twelve (12) loading scenarios on the cylinders, $S_1 = 0$ MPa– $S_{12} = 22.32$ MPa, with an interval of 2.03 MPa. The applied stress was gradually increased with a constant loading interval, which was controlled by MTS multipurpose test software. Time intervals were set as 3 minutes for stress increase and 4.5 minutes for EMI measurement. For each loading case, the loading rate was controlled at a constant speed of $0.0113 \text{ MPa} \cdot \text{s}^{-1}$. The total time for a complete loading history on a concrete cylinder was 97 minutes, including 10 minutes for unloading at the end. Note that no surface crack was observed for the applied stress during the compression tests for cylinders 1–3.

The harmonic excitations were set at the amplitude of 1 V to measure EMI signals from the SAs 1–3. The EMI signals were swept in the frequency range from 100 kHz to 600 kHz with 500 intervals (i.e., to measure at 501 points in

the frequency band). Four ensembles of the measurement were recorded for each loading case. The monitored temperature varied from 22°C to 23°C (around a variation of 1°C). Thus, the effect of the temperature alteration on the EMI signatures could be ignored.

3.4. EMI Signatures. Figure 10 shows the raw EMI signals of the SAs 1–3 recorded for the 12 loading cases (S_1 – S_{12}). The signals were measured in the frequency band of 100–600 kHz. The EMI signals exhibit three prominent resonant peaks (peaks 1–3) for each SA sensor. As shown in Figure 10(a), SA 1 had 231 kHz (Peak 1), 285 kHz (Peak 2), and 502 kHz (Peak 3). In the figure, the EMI responses were insignificantly changed from S_1 (0 MPa) to S_7 (12.18 MPa around $0.48\sigma_c$). The EMI responses were suddenly varied at S_8 (14.21 MPa around $0.56\sigma_c$), thus indicating a transformation of the concrete domain (e.g., inner concrete damage [7, 17, 54]) surrounding SA 1 in the concrete cylinder 1. The EMI responses were continuously altered under applied stresses S_9 – S_{12} .

As shown in Figure 10(b), SA 2 had 216 kHz (Peak 1), 273 kHz (Peak 2), and 498 kHz (Peak 3). In the figure, the EMI responses showed minimal variation between S_1 (0 MPa) and S_7 (12.18 MPa). However, there was an abrupt alteration in EMI frequency at S_8 (14.21 MPa around $0.56\sigma_c$), which could be induced by inner damage in the concrete cylinder 2 [7, 17, 54]. The EMI responses were continuously changed under applied stresses S_9 – S_{12} .

As shown in Figure 10(c), SA 3 had 212 kHz (Peak 1), 269 kHz (Peak 2), and 480 kHz (Peak 3). According to the figure, there were insignificant variations in the EMI responses between S_1 and S_7 . However, at S_8 , a sudden alteration in EMI responses occurred, which could be caused by internal damage in the concrete cylinder 3 [7, 17, 54]. The EMI responses of SA 3 continuously varied under S_8 , and it underwent other abrupt variations under stress S_{12} (transformation from inner damage to surface crack).

In the case of concrete structures under compressive forces, internal damage to the concrete, often manifesting as inner cracks, may occur prior to the appearance of surface cracks, as indicated by previous studies [7, 17, 54–57]. Via the observations in Figure 10, it can be concluded that the sudden changes in impedance responses of the SAs 1–3 could be induced by the inner damage in the concrete specimens.

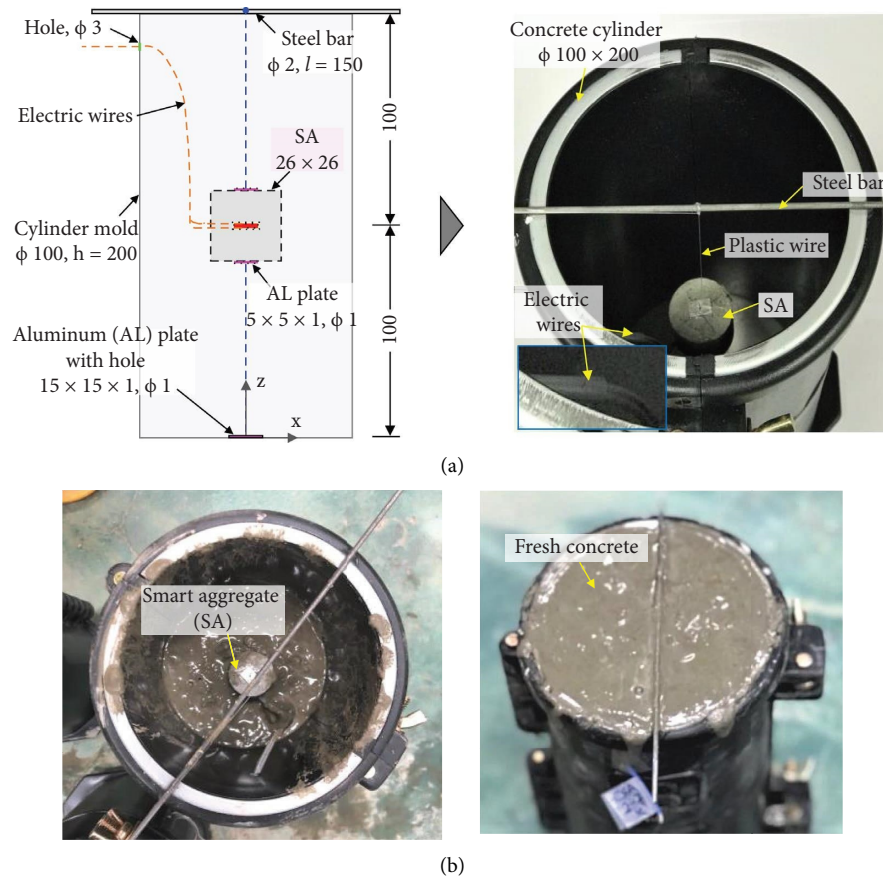


FIGURE 7: Fabrication of SA-embedded concrete cylinder. (a) Localization of SA in cylinder specimen (dimension in mm). (b) Concrete casting.

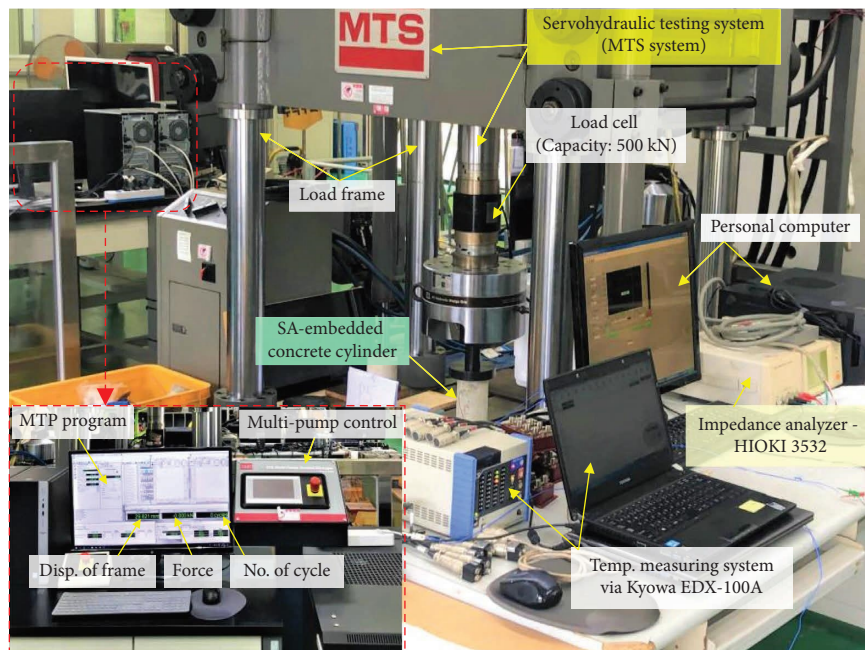


FIGURE 8: Testing setup for EMI measuring from SA-embedded concrete cylinder under the compression test.

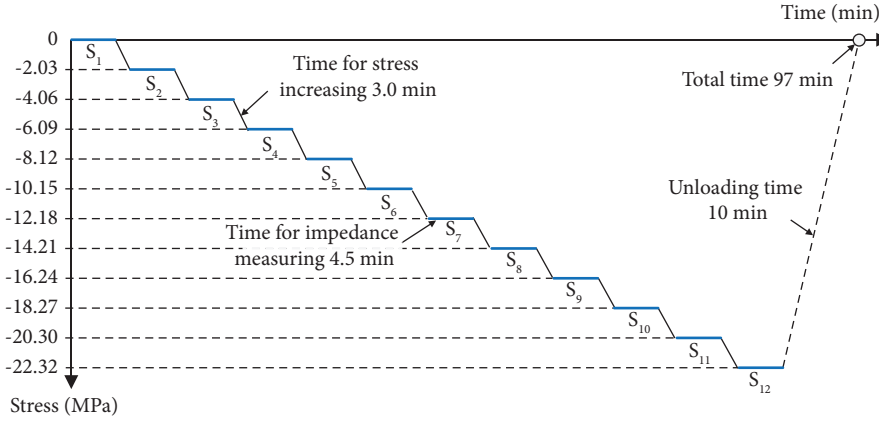


FIGURE 9: Applied loading history on the cylinder.

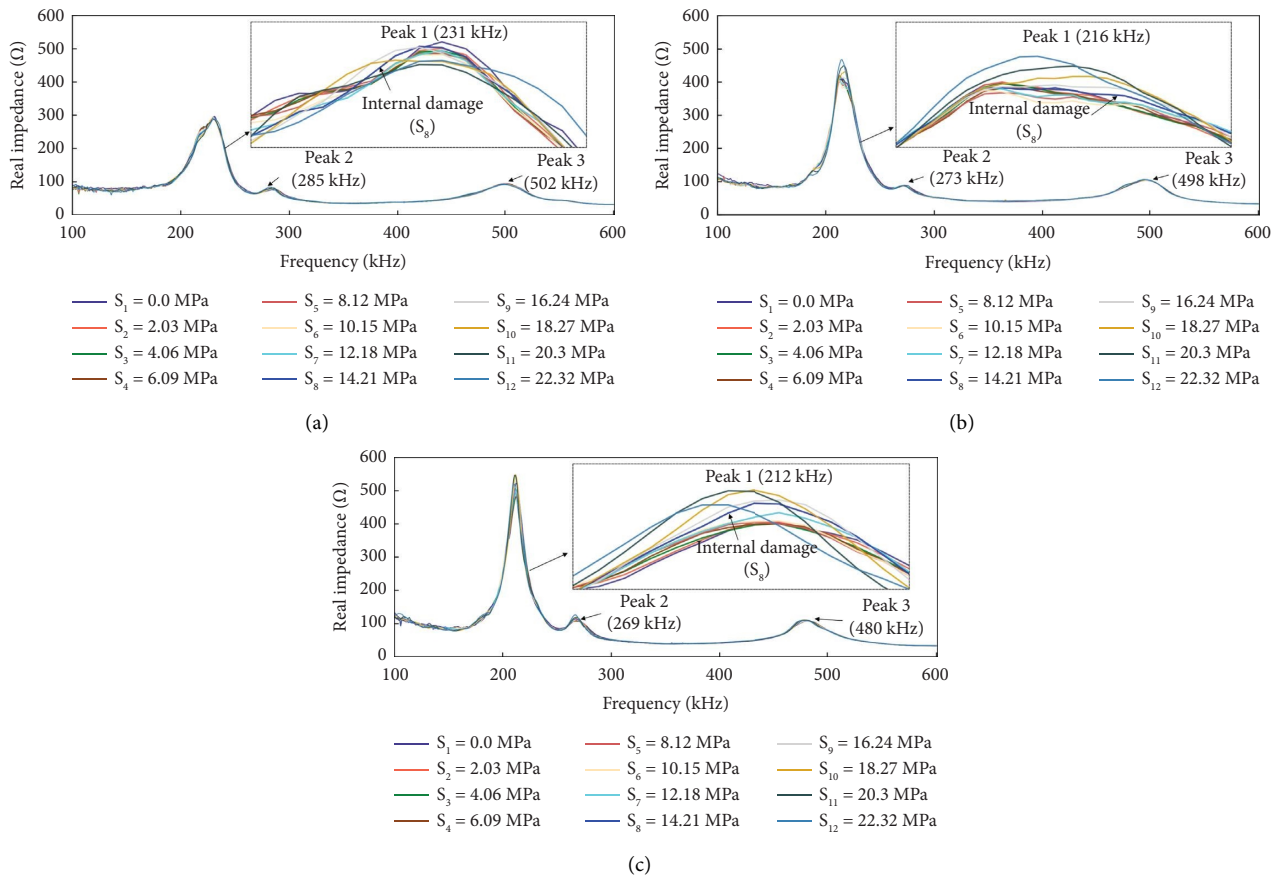


FIGURE 10: Raw EMI signals of SAs 1–3 under various applied stresses. (a) SA 1. (b) SA 2. (c) SA 3.

There were differences in the raw EMI signals of SAs 1–3. These differences could be induced by the sensor fabrication process (e.g., epoxy layer thickness or concrete distribution around the PZT sensor [56, 58]), the SA-embedded cylinder fabrication (dissimilar distribution of concrete mixture surrounding the SA sensors in the three-cylinder samples), and the conditions during the compression test (contact surface between the tested cylinder and upper and bottom plates of MTS machine). As observed in the figure, the raw EMI signals of SAs 1–3 were insignificantly changed under increasing applied stresses,

except for the sudden alteration in SA 3's signals under the applied stress case S_{12} . The sudden variation in SA 3's raw EMI signatures under the last loading case (S_{12}) could be attributed to the transformation of the concrete medium around SA 3 [7].

3.5. Statistical EMI Quantification. Figures 11 and 12 show the computed statistical features, RMSD and CCD indices [38, 59], to quantify the variations in raw EMI signals under various applied stresses (S_1 – S_{12}). The whole measured range

of 100–600 kHz was employed for these computations. The upper control limit, UCL [59], was also calculated to aid in decision-making. It is computed by three standard deviations of the mean (99% confidence level). Any quantified index surpassing the UCL value indicates the presence of changes in the applied stress level. It can be seen that both RMSD (see Figure 11) and CCD (see Figure 12) indices were below the UCL line under the intact case ($S_1 = 0$ MPa). These indices increased and surpassed the UCL line under the following cases (S_2 – S_{12}).

Figure 11 shows the RMSD indices of SAs 1–3 corresponding to all stress levels applied to three cylinders (cylinders 1–3). There were differences in the RMSD values of these SA sensors (SAs 1–3) (see Figure 11). It could be induced by the uncertainties during the sensor fabrication, the SA-embedded cylinder construction, and the compression test setup. The RMSD indices did not consistently increase with some increasing applied stress levels. For example, for SA 1, the RMSD index under $S_4 = 6.09$ MPa (2.9%) was smaller than that under $S_3 = 4.06$ MPa (3.1%); for SA 2, the RMSD indices under stress cases $S_5 = 8.12$ MPa, $S_7 = 12.18$ MPa, and $S_8 = 14.21$ MPa were the same at 4%; and for SA 3, the RMSD reduced from 4.3% (under S_6) to 4.2% (under S_7).

Furthermore, it can be noted that the RMSD indices of SAs 1–3 had a change in the pattern. They were abruptly changed under S_8 and then increased from S_8 to S_{12} . These variations could be caused by the inner damage surrounding the SA sensors (SAs 1–3) in the concrete specimens (the cylinders 1–3) [7, 17, 54]. The RMSD index of SA 3 also underwent a sudden increase when the applied stress transitioned from S_{11} to S_{12} , thus revealing a transformation from inner damage to the surface crack of cylinder 3.

Figure 12 shows the CCD indices of SAs 1–3. The magnitudes of CCD were insignificantly increased under increasing applied stress levels (S_2 – S_{12}). These indices were nearly unchanged under stresses S_1 – S_7 for three SAs 1–3 (see Figure 12). Moreover, for SAs 1–3, the CCD indices were altered under S_8 and then increased from S_8 to S_{12} . These alterations could be induced by the internal damage surrounding the SAs 1–3 in the cylinders 1–3 [7, 17, 54]. The CCD index of SA 3 also abruptly altered under stress level S_{12} , thus suggesting a transformation from internal damage to a surface crack of cylinder 3.

Based on the analysis of the statistical metrics, it is evident that the RMSD indices exhibited higher sensitivity to the change in stress levels compared to the CCD indices (see Figures 11 and 12). However, the RMSD values were not consistently increased in a gradual manner for certain applied stress levels. It is noticed that more reliable techniques should be implemented to accurately analyze EMI features of the SAs 1–3 corresponding to the applied loading levels.

4. Performance Evaluation

4.1. Stress Evaluation Using K-Fold Cross-Validation

4.1.1. Databank Configuration. Figure 13 shows the raw EMI signals recorded for the 12 stress levels (i.e., S_1 – S_{12}) of SAs 1–3. Corresponding to each stress level, the raw EMI

signals of each SA sensor were recorded by four ensembles. It means 12 signals were obtained for three SAs per stress level. A total of 144 raw EMI signals were acquired after experiments.

Figure 14 visualizes the measured EMI datasets in twelve stress levels. As presented in Section 3.3, each raw EMI signal (i.e., one ensemble) was recorded with 501 data points. Corresponding to 12 EMI signals, there were 6012 data points recorded per stress level and were presented in a specific color. As a result, 72144 data points were obtained corresponding to 12 stress levels used for the 1D CNN model.

The stratified shuffle-split technique was utilized to generate data for fold datasets, as mentioned in Section 2.4. Of the 12 raw EMI signals obtained from SAs 1–3 at each stress level, 9 signals were assigned randomly to the training fold dataset, and 3 remaining signals were assigned to the evaluation fold dataset. Via the stratified shuffle-split technique, the same ratio could be set to maintain consistency in a single layer step (stress step) for both the 1D CNN training and evaluation fold datasets. In addition, we ensured that all split datasets generated through the shuffle-split technique were different from each other. In summary, there were 144 signals in the EMI dataset, of which 108 and 36 signals were used for 1D CNN training and evaluation, respectively.

4.1.2. Training and Testing Results. This section shows training procedures and evaluation results of the 1D CNN deep learning model (as described in Table 1) via the 10-fold cross-validation. The model was trained on the training fold datasets, and then it was tested on corresponding evaluation fold datasets. The final performance of the proposed model was confirmed via averaging the results from 10-folds. Besides, performance comparison of different 1D CNN architectures was also investigated in Appendix A.

(1) Training Procedures. A desktop computer (GPU—GeForce GT 2080 Ti of 11 GB, CPU—Intel Core i9-9000 KF of 3.6 GHz, RAM—64 GB) performed all computations. The 1D CNN deep learning model was built using Python language [60], and it was trained by using the Adam optimizer algorithm [61] with a mini-batch size of 1 and a learning rate of 0.001.

Figures 15 and 16 depict the training process of the 1D CNN deep learning model using the training fold datasets. Among 10 folds mentioned in Section 2.4, folds 1 and 4 were selected to plot because these folds provided an efficient learning performance for the 1D CNN model. Figure 15 shows a gradual drop in both training loss and validation loss within the first 25 epochs, followed by a steady convergence after 100 epochs. Figure 16 shows a sharp decrease in training RMSE and validation RMSE within the initial 15 epochs and then continuing to converge until the end of the learning process. The observed loss and RMSE values indicated that the proposed 1D CNN model performs well.

(2) Testing Result. Figure 17 shows the stress evaluation results of the 1D CNN deep learning model on evaluation fold datasets for 10 folds. In Figure 17(a), fold 1 had

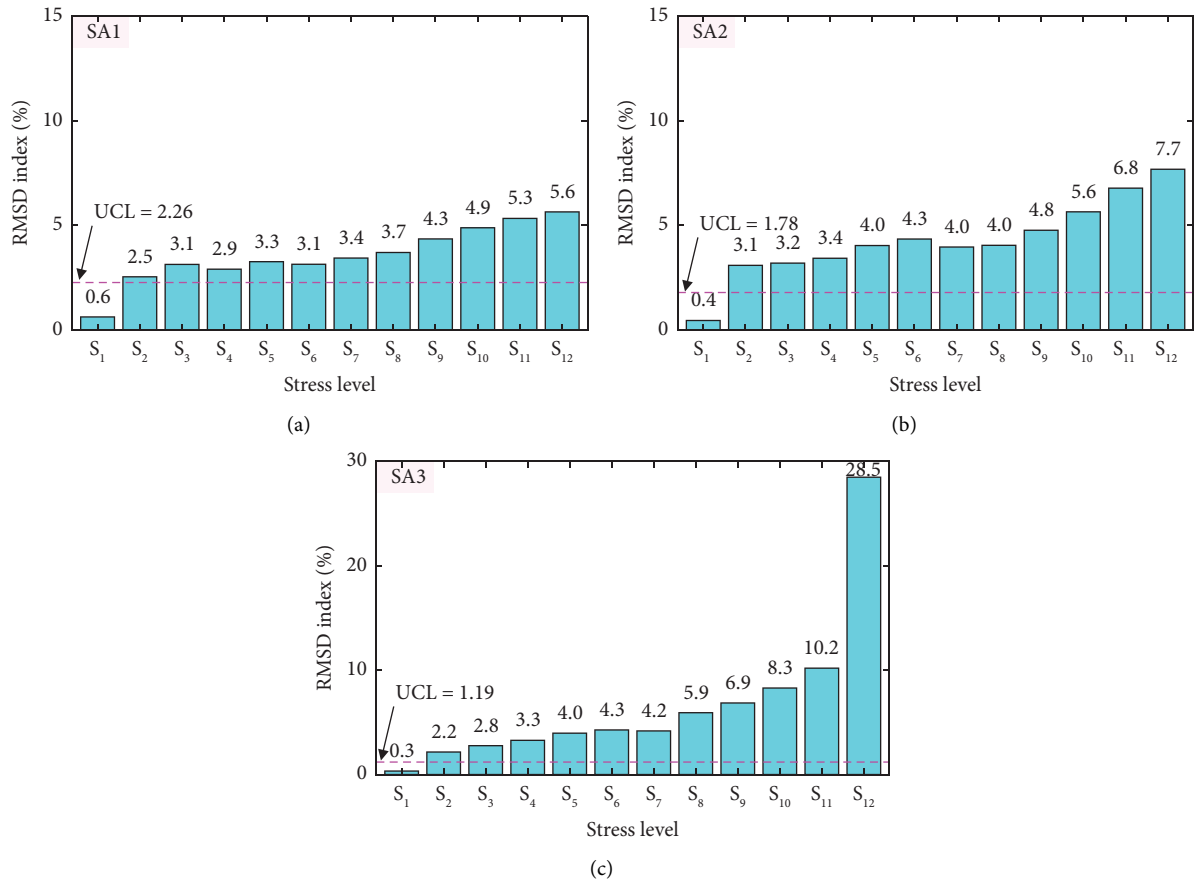


FIGURE 11: RMSD indices of SAs 1–3 under various applied stresses. (a) SA 1. (b) SA 2. (c) SA 3.

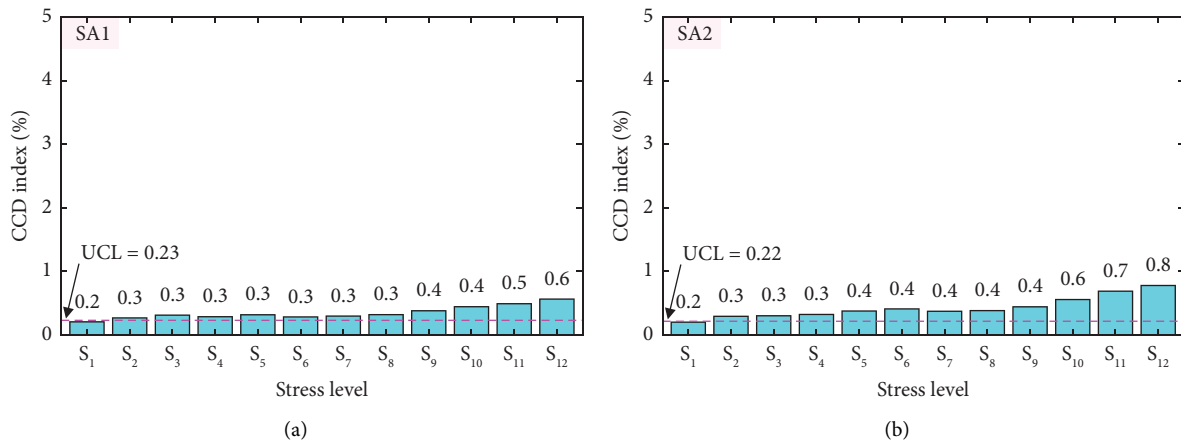


FIGURE 12: Continued.

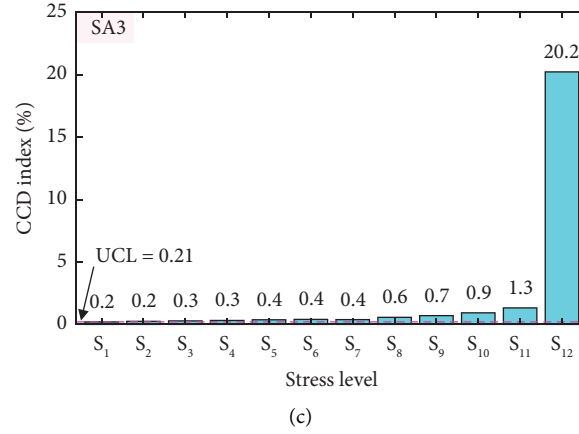


FIGURE 12: CCD indices of SAs 1–3 under various applied stresses. (a) SA 1. (b) SA 2. (c) SA 3.

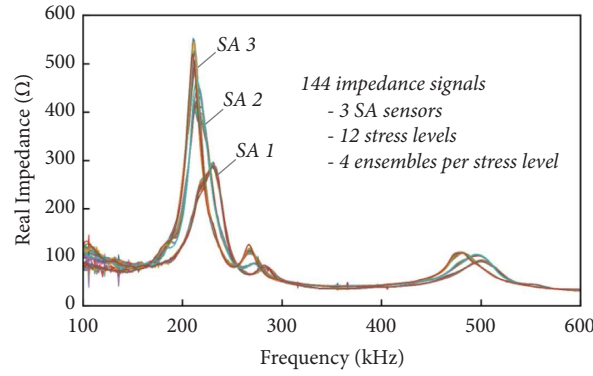


FIGURE 13: Raw EMI signals of SAs 1–3 measured for 12 stress levels.

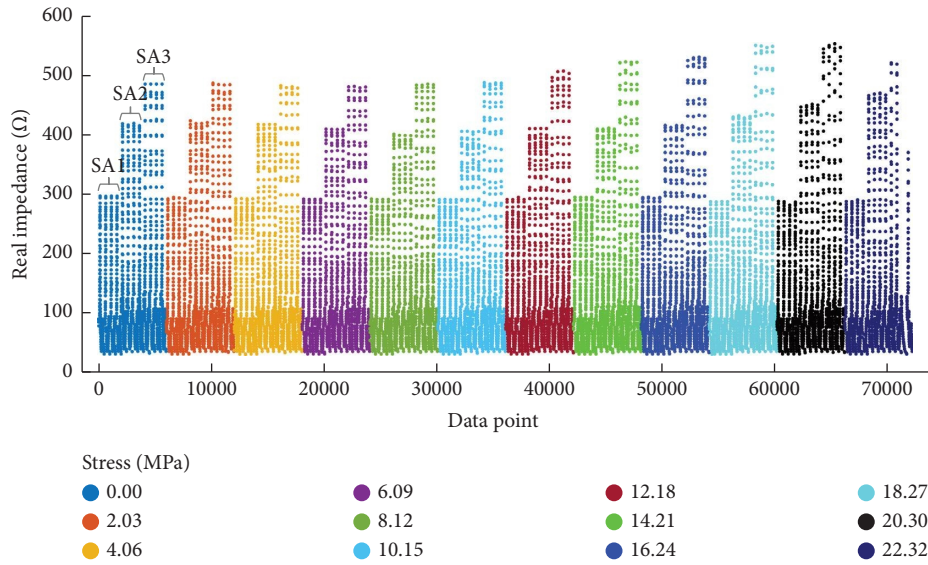


FIGURE 14: Visualization of EMI datasets for 12 stress levels of SAs 1–3.

RMSE = 0.85, which meant the stress could be predicted on its evaluation fold dataset by the error of 0.85 MPa. In Figure 17(d), fold 4 had RMSE = 0.94, which meant the stress

could be predicted on its evaluation fold dataset by the error of 0.94 MPa. Figure 17(k) presents the RMSE values of 10 evaluation fold dataset and their average. The RMSE values

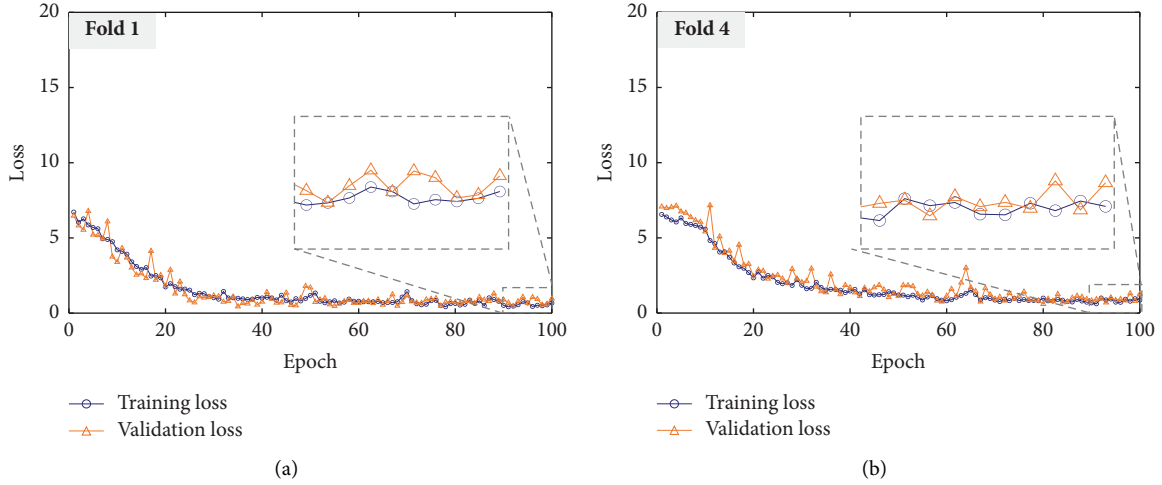


FIGURE 15: Loss values of 1D CNN deep learning model after 100 epochs. (a) Fold 1. (b) Fold 4.

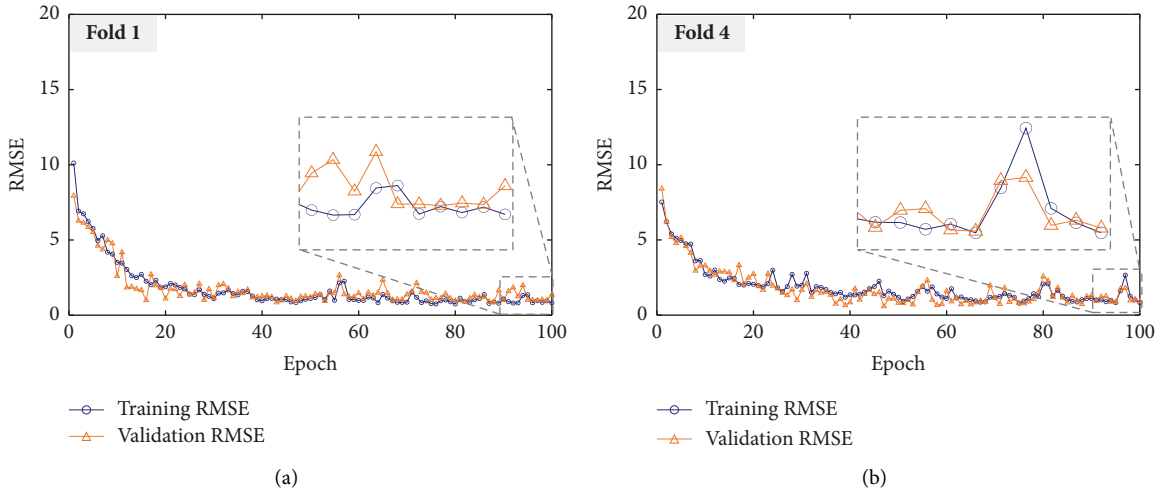


FIGURE 16: RMSE values of 1D CNN deep learning model after 100 epochs. (a) Fold 1. (b) Fold 4.

ranged from 0.85 to 2.14 for the whole evaluation fold dataset, in which the lowest and highest errors were shown at fold 1 and fold 8, respectively. The average RMSE was 1.38, meaning the 1D CNN deep learning model could predict stress by an average error of 1.38 MPa.

Figure 18 presents the average performance of the trained 1D CNN deep learning model across 10 folds. As shown in Figure 18(a), the average predicted stress results on the evaluation datasets of 10 folds were plotted. It is observed that the average predicted stress in each stress level was quite consistent with the actual stress. In Figure 18(b), the mean of predicted stress shown in Figure 17 was calculated to provide a more stable and reliable estimate. The mean of predicted stress values exhibited a good agreement with the actual stress levels, with the exception of stress level S_1 . The mean of prediction stress values for S_1 was remarkably close to those for S_2 (as shown in Figure 18(b)). This observation could potentially be influenced by the initial boundary condition during the implementation of the compression tests on concrete cylinders.

4.2. Stress Prediction on Noise-Contaminated Databank

4.2.1. Databank Configuration. The EMI signatures obtained from the PZT sensors in real applications are indeed altered by external disturbances such as noise conditions [62–64]. To evaluate the performance of the 1D CNN deep learning model under different noise levels, a noise-contaminated databank was created by injecting the Gaussian noise (described in Section 2.4) into the raw EMI signals of SA 2. To construct the training databank, the raw EMI signals underwent random noise addition with standard deviations of 0%, 1%, 2%, 3%, 4%, and 5% of the signal amplitude. For each of the 12 stress levels, three raw signals (selected from four ensembles) were augmented with random noise, resulting in a total of 216 signals for training the 1D CNN model.

To generate the testing databank, the remaining raw signal of each stress level was injected by various noise levels ranging from 1% to 16%, with an interval of 1%. This process aimed to assess the reliability and generalization of the 1D CNN model on unseen test data. In each noise level, the 120

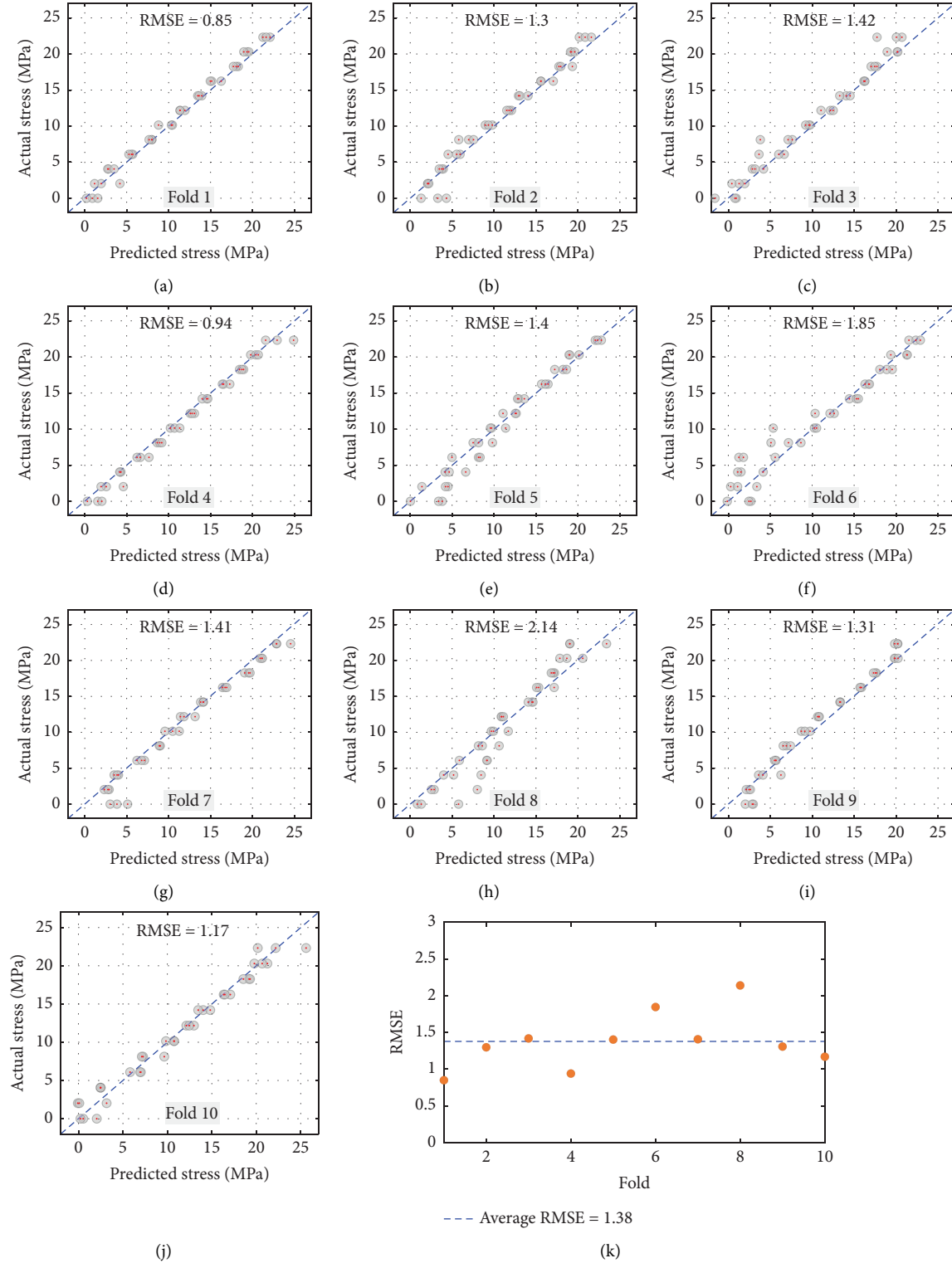


FIGURE 17: Stress evaluation results of 1D CNN deep learning model. (a) Fold 1. (b) Fold 2. (c) Fold 3. (d) Fold 4. (e) Fold 5. (f) Fold 6. (g) Fold 7. (h) Fold 8. (i) Fold 9. (j) Fold 10. (k) RMSE.

new signals were generated for twelve stress levels (i.e., 10 new signals for each stress level). It resulted in a total of 1,920 signals generated for the 16 noise levels. Consequently, the testing databank comprised a total of 1,932 signals, which included the original 12 measured raw EMI signals with 0%

noise. Figure 19 illustrates examples of raw EMI signals at stress level S_1 with added noise. Overall, the training databank consisted of 216 signals, while the testing databank included 1,932 signals, enabling evaluation of the 1D CNN model's performance under different noise levels.

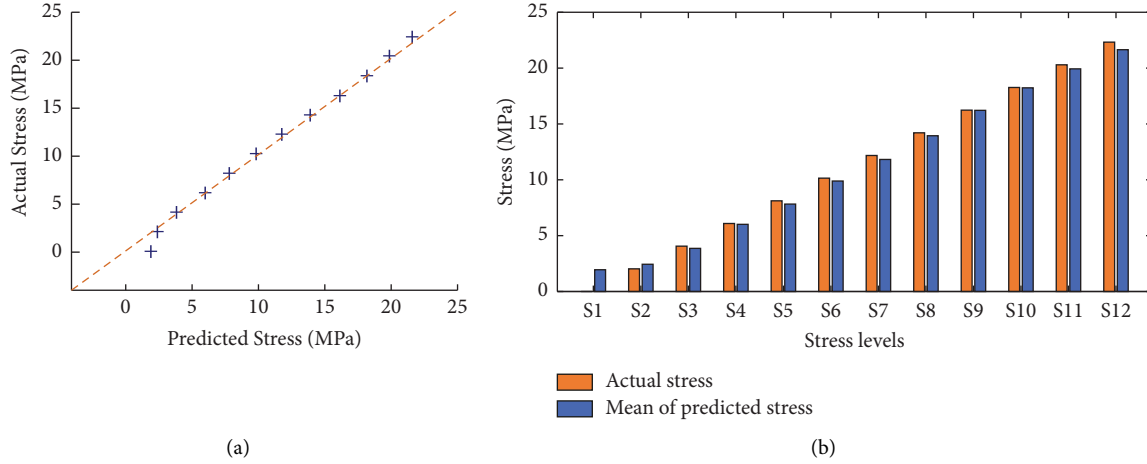


FIGURE 18: Average performance of trained 1D CNN deep learning model. (a) Stress evaluation. (b) Actual stress vs. predicted stress.

4.2.2. Training Process. Figure 20 shows the loss and RMSE values of the 1D CNN deep learning model after 100 epochs. The model was trained on the 216 signals (as described in the previous section). Figure 20(a) presents the training and validation loss values. The training loss exhibited a sharp decrease in the initial ten epochs and gradually converged towards the end of the learning process (100th epoch). The validation loss significantly fluctuated with a downward trend in the first twenty epochs and continued to fluctuate slightly until the end. It is noticed that the selected model achieved a training loss of approximately 0.71 at the 74th epoch, which corresponded to the lowest validation loss of around 0.89.

Figure 20(b) displays the training and validation RMSE values. Similar to the training loss, the training RMSE showed a rapid decline in the first ten epochs and reached convergence by the 100th epoch. Like the validation loss, the validation RMSE varied with a downward trend in the first twenty epochs, followed by slight fluctuations until the end. Specifically, the training RMSE value was around 0.88 at the 74th epoch, corresponding to the lowest validation RMSE of about 1.14.

4.2.3. Stress Prediction Results. Figure 21 shows the effects of noise on the accuracy of the 1D CNN deep learning model. The predicted stress values were compared with the actual values for various noise levels. As depicted in this figure, the accuracy of stress prediction diminished as the noise level increased.

Figure 22 shows linear relationships between the RMSE index and noise levels. Figure 22(a) displays the trained noise levels ranging from 0% to 5%, while Figure 22(b) represents the untrained noise levels ranging from 6% to 16%. It is evident that the RMSE values exhibited a linear increase corresponding to higher percentages of noise. The accuracy of the 1D CNN model was affected by the noise level, and this relationship could be adjusted using empirical functions. In summary, both Figures 21 and 22 emphasize the

adverse influence of noise on the accuracy of the 1D CNN model, highlighting the need to consider and mitigate noise effects in order to improve model performance.

4.3. Stress Prediction for Untrained Stress Levels

4.3.1. Databank Configuration. The robustness of the 1D CNN deep learning model was investigated for stress monitoring using partially untrained EMI data. As explained in Section 2.4, the training databank was generated by excluding EMI datasets corresponding to specific stress levels. In this case, the 216 signals from SA 2, described in Section 4.2.1, were utilized to construct three distinct training datasets. Table 4 presents the design of the three training datasets as follows: (1) training dataset 1 (198 signals): This dataset excluded stress level S_4 from the initial 216 signals; (2) training dataset 2 (180 signals): this dataset excluded stress levels S_4 and S_6 from the initial 216 signals; and (3) training dataset 3 (162 signals): this dataset excluded stress levels S_4 , S_6 , and S_9 from the initial 216 signals.

Three training datasets were used to train three separate 1D CNN models. These models were evaluated using the testing dataset (216 signals) which included stress levels S_4 , S_6 , and S_9 . By evaluating the performance of the 1D CNN models on the testing dataset, the study aimed to assess the robustness of the models when confronted with partially untrained EMI data, specifically with the exclusion of certain stress levels.

4.3.2. Training Process. Figure 23 shows the loss and RMSE values of the 1D CNN deep learning model trained using the training dataset 1, which excluded stress S_4 . In Figure 23(a), the training loss exhibited a rapid reduction in the initial ten epochs, followed by a gradual decrease up to the 60th epoch and then continued to decrease with slight fluctuations from the 61st to the 100th epoch. The validation loss experienced a sharp drop with significant variations in the first seven epochs. The validation loss fluctuated and reached its lowest

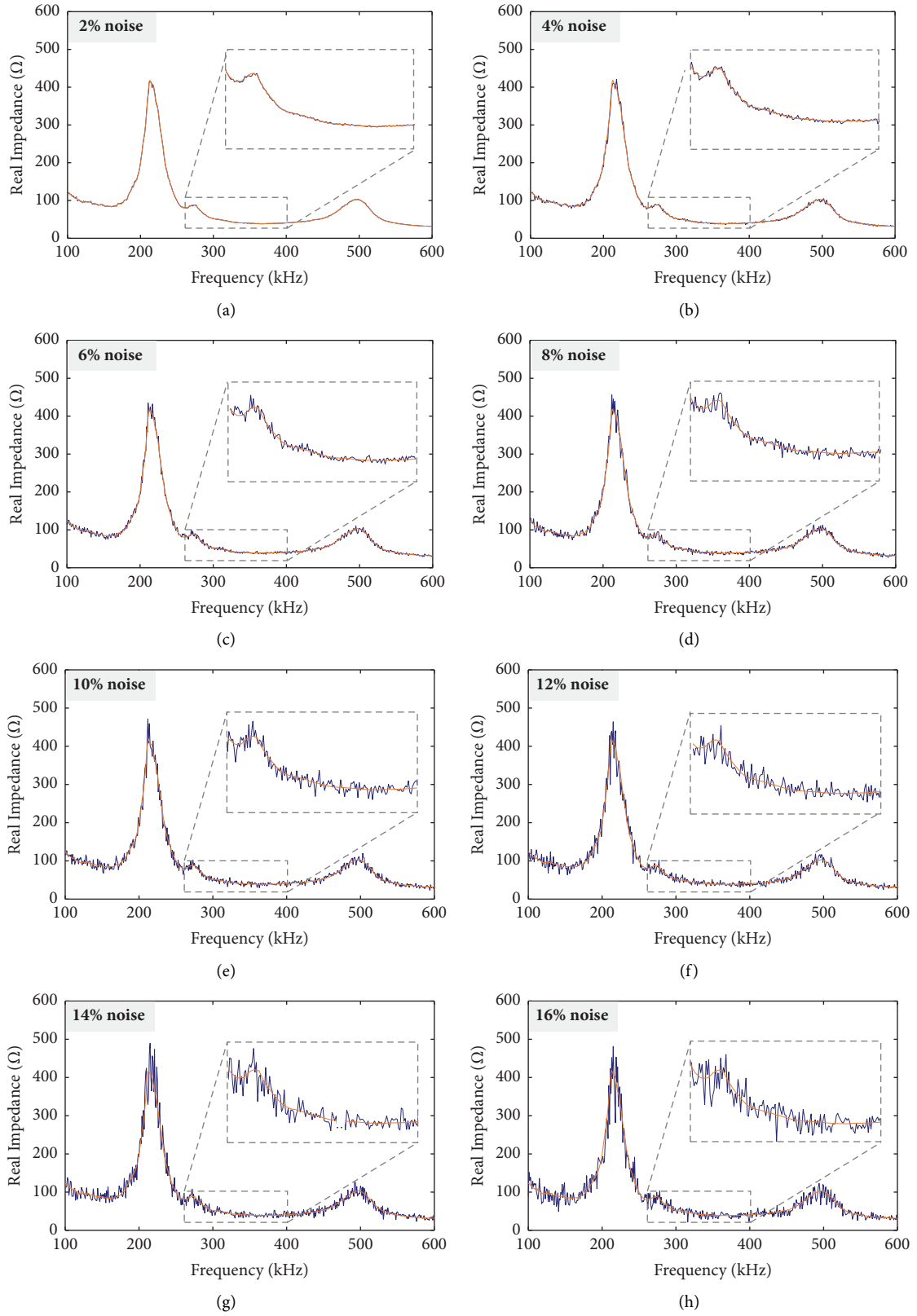


FIGURE 19: Noise injection to raw EMI signals for data argumentation (stress level S_1). (a) 2% noise. (b) 4% noise. (c) 6% noise. (d) 8% noise. (e) 10% noise. (f) 12% noise. (g) 14% noise. (h) 16% noise.

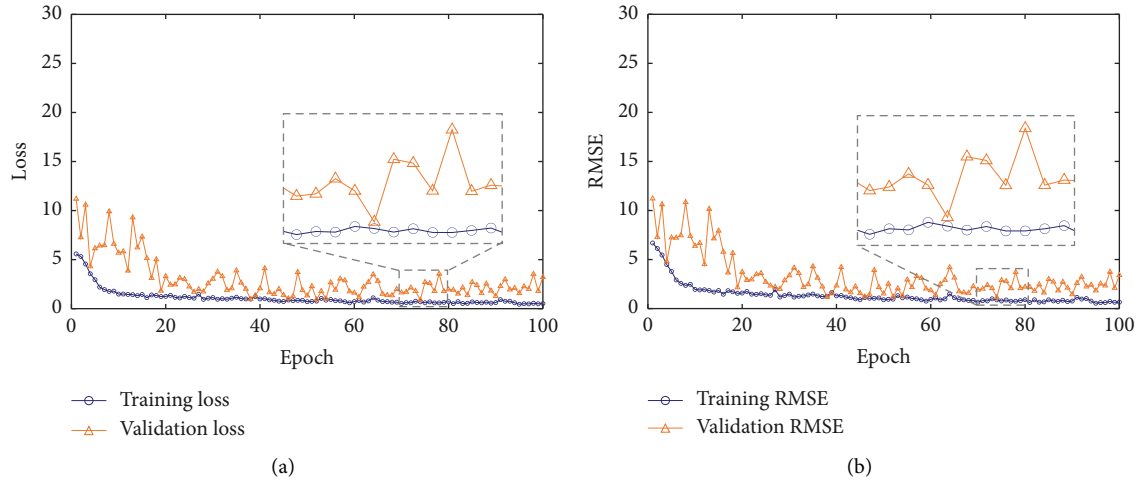


FIGURE 20: Loss and RMSE values of 1D CNN deep learning model after 100 epochs. (a) Loss. (b) RMSE.

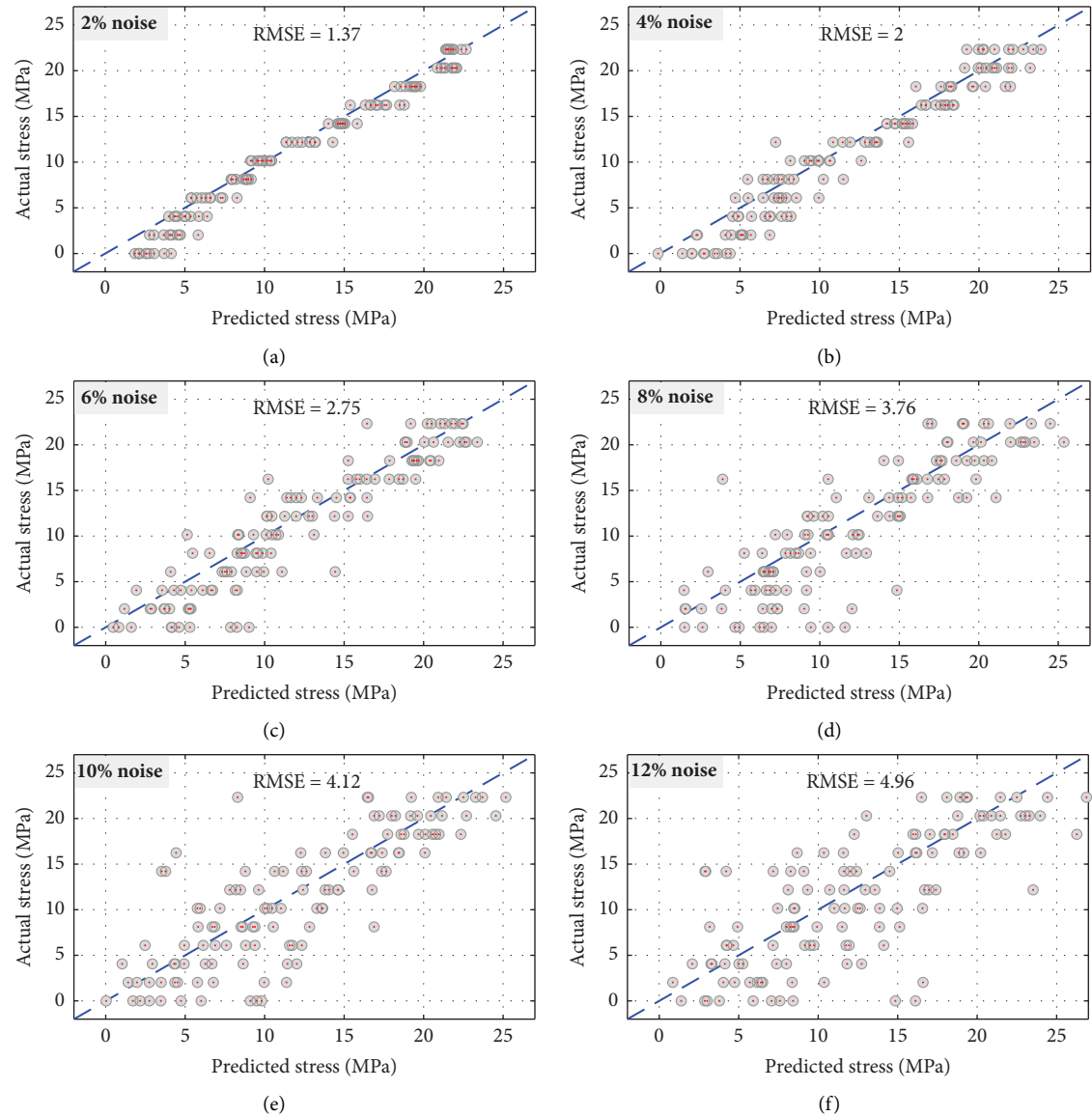


FIGURE 21: Continued.

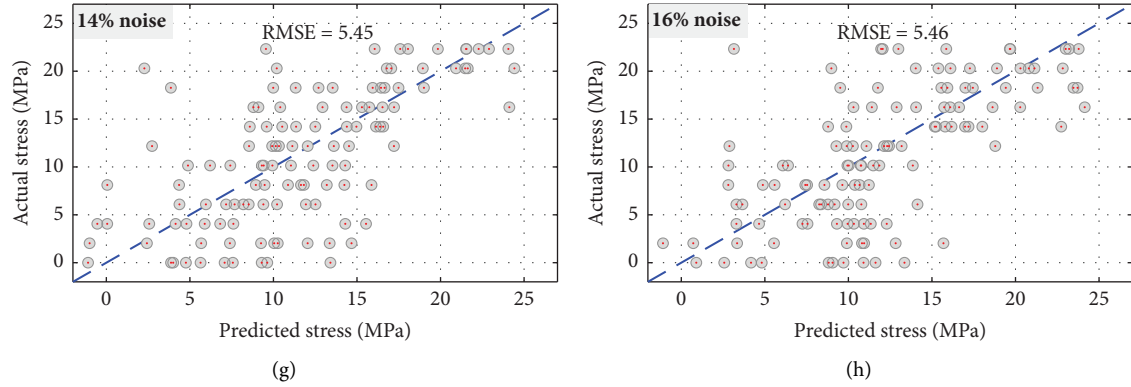


FIGURE 21: Effects of noises on the accuracy of 1D CNN deep learning model. (a) 2% noise. (b) 4% noise. (c) 6% noise. (d) 8% noise. (e) 10% noise. (f) 12% noise. (g) 14% noise. (h) 16% noise.

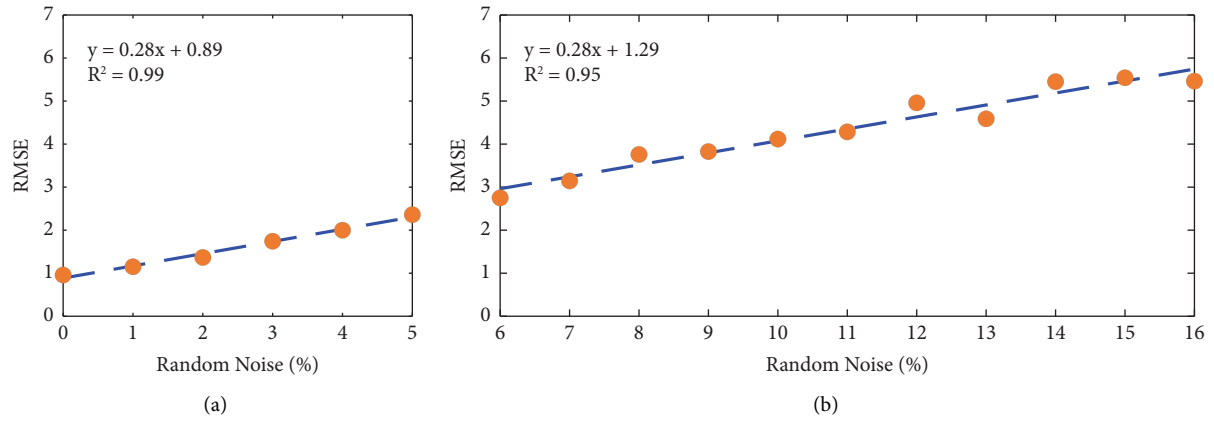


FIGURE 22: Relation between RMSE and noise levels. (a) Trained levels of noise (0%–5%). (b) Untrained levels of noise (6%–16%).

TABLE 4: Dataset scenarios for evaluating the performance of the 1D CNN deep learning model.

	Training dataset			Testing dataset
	Training dataset 1 (excluded S_4)	Training dataset 2 (excluded S_4, S_6)	Training dataset 3 (excluded S_4, S_6, S_9)	
Signal number	198	180	162	216

point at the 41st epoch, followed by slight fluctuations until the end of the learning process. It is noted that the selected model achieved a training loss of approximately 0.73 at the 41st epoch, corresponding to the lowest validation loss of nearly 1.14.

Figure 23(b) shows the training and validation RMSE. The training RMSE rapidly decreased in the initial ten epochs and continued to decrease with slight variations throughout the 100-epoch training process. The validation RMSE exhibited a rapid decline with high variations in the first seven epochs. Afterwards, the validation RMSE underwent fluctuations until the end of the learning process. It

is observed that the training RMSE of the predicted stress and actual values was approximately 0.97 at the 41st epoch, corresponding to the lowest validation RMSE of nearly 1.34.

4.3.3. Stress Prediction Results. Three 1D CNN deep learning models were evaluated on training datasets 1–3, and their results are shown in Figures 24–26. The figures indicated a good agreement between predicted and actual stresses, suggesting the models' ability to accurately predict untrained stress levels.

Comparing the RMSE values, there were slight differences between excluded and included stress levels.

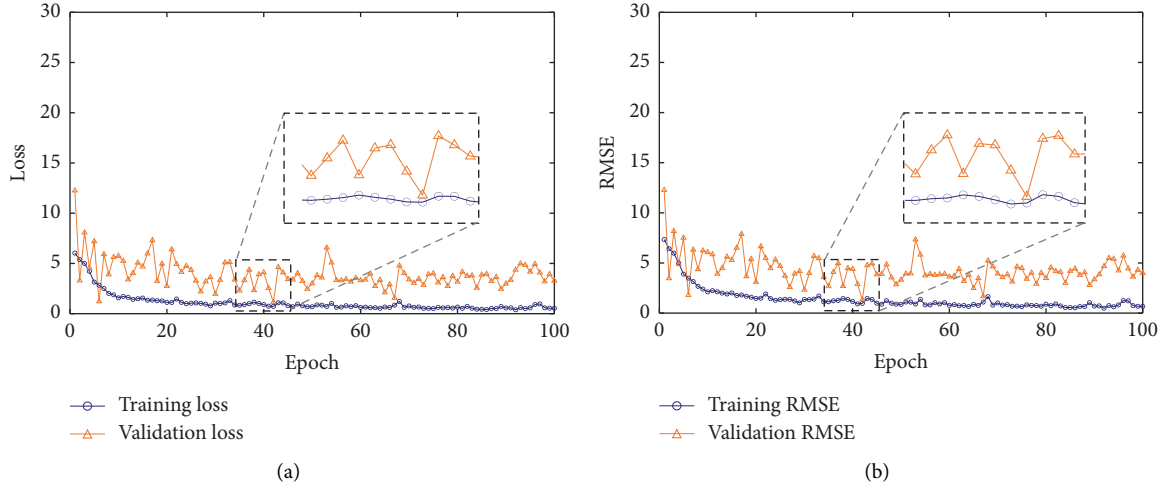


FIGURE 23: Loss and RMSE values of 1D CNN deep learning model trained by training dataset 1 (excluded stress S_4). (a) Loss. (b) RMSE.

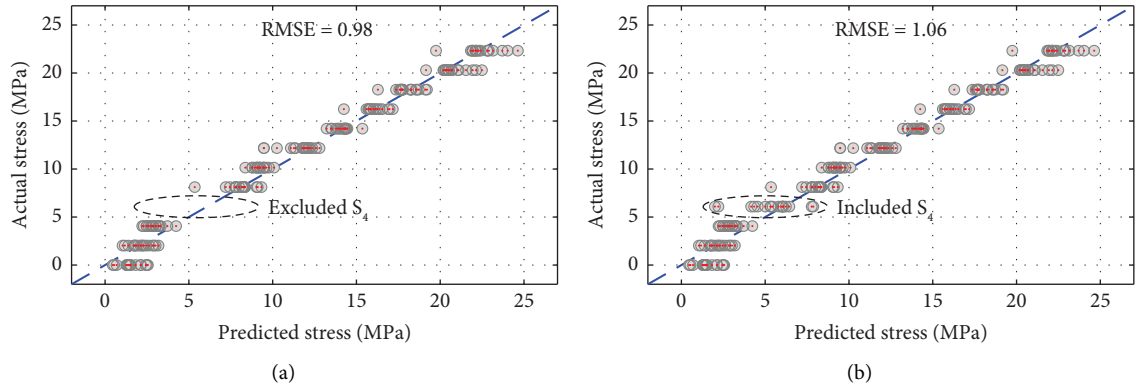


FIGURE 24: Stress prediction on the training dataset 1 (std: 0–5%). (a) Excluded S_4 . (b) Included S_4 .

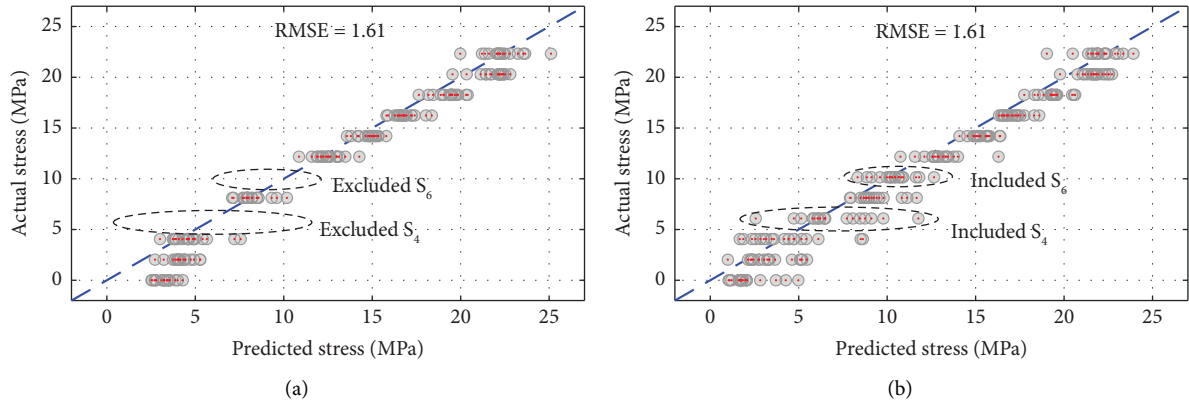


FIGURE 25: Stress prediction on the training dataset 2 (std: 0–5%). (a) Excluded $S_{4,6}$. (b) Included $S_{4,6}$.

Prediction errors increased when more stress levels were excluded from the training dataset. However, the RMSE value for dataset 2 was slightly higher than that of dataset 3, possibly due to the nonlinear characteristics of EMI

responses. In addition, selecting the trained models at their best epochs could be the reason.

Overall, these results confirm the effectiveness of the proposed 1D CNN model in accurately predicting stress

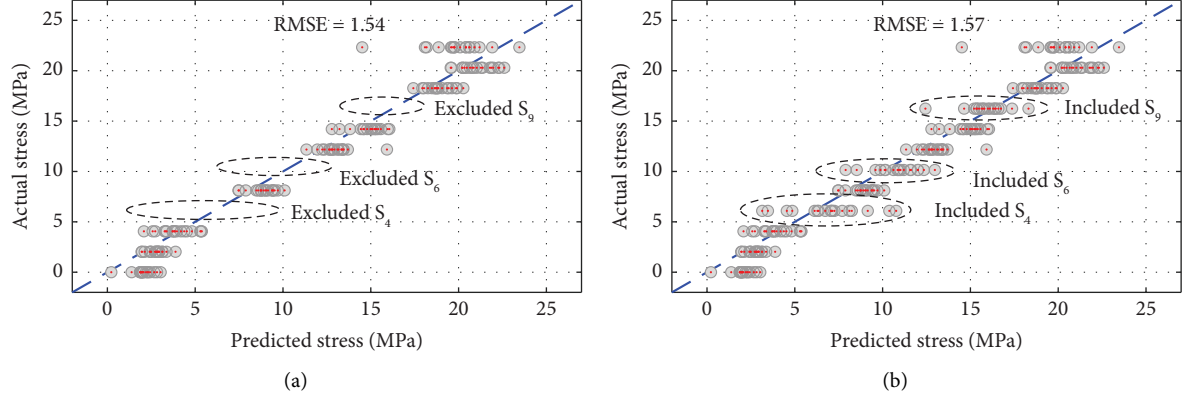


FIGURE 26: Stress prediction on the training dataset 3 (std: 0–5%). (a) Excluded $S_{4,6,9}$. (b) Included $S_{4,6,9}$.

TABLE 5: Specifications of the four 1D CNN architectures (M1 – M4).

Layers	Type	Depth	Filter	Stride
<i>Model M1</i>				
1	Conv	4	1×6	1
2	ReLU	—	—	—
3	Maxpool	—	1×2	2
4	Conv	4	1×4	1
5	ReLU	—	—	—
6	Maxpool	—	1×2	2
7	Conv	8	1×5	1
8	ReLU	—	—	—
9	Maxpool	—	1×2	2
10	Fc ₁	48	—	—
11	Fc ₂	32	—	—
12	Fc ₃	1	—	—
13	Regression	—	—	—
<i>Model M2</i> (see Table 1)				
<i>Model M3</i>				
1	Conv	4	1×6	1
2	ReLU	—	—	—
3	Maxpool	—	1×2	2
4	Conv	4	1×4	1
5	ReLU	—	—	—
6	Maxpool	—	1×2	2
7	Conv	8	1×5	1
8	ReLU	—	—	—
9	Maxpool	—	1×2	2
10	Conv	8	1×5	1
11	ReLU	—	—	—
12	Maxpool	—	1×2	2
13	Conv	8	1×5	1
14	ReLU	—	—	—
15	Maxpool	—	1×2	2
16	Fc ₁	48	—	—
17	Fc ₂	32	—	—
18	Fc ₃	1	—	—
19	Regression	—	—	—
<i>Model M4</i>				
1	Conv	4	1×6	1
2	ReLU	—	—	—
3	Maxpool	—	1×2	2
4	Conv	4	1×4	1

TABLE 5: Continued.

Layers	Type	Depth	Filter	Stride
5	ReLU	—	—	—
6	Maxpool	—	1×2	2
7	Conv	8	1×5	1
8	ReLU	—	—	—
9	Maxpool	—	1×2	2
10	Conv	8	1×5	1
11	ReLU	—	—	—
12	Maxpool	—	1×2	2
13	Conv	8	1×5	1
14	ReLU	—	—	—
15	Maxpool	—	1×2	2
16	Conv	8	1×5	1
17	ReLU	—	—	—
18	Maxpool	—	1×2	2
19	Fc ₁	48	—	—
20	Fc ₂	32	—	—
21	Fc ₃	1	—	—
22	Regression	—	—	—

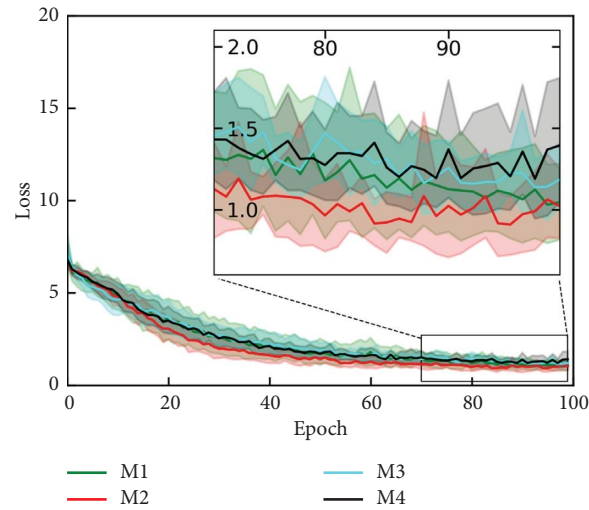


FIGURE 27: Training loss of the four 1D CNN architectures (M1–M4).

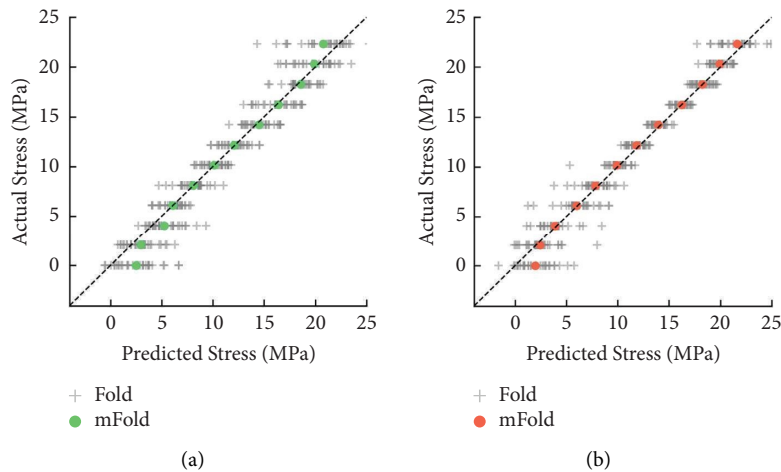


FIGURE 28: Continued.

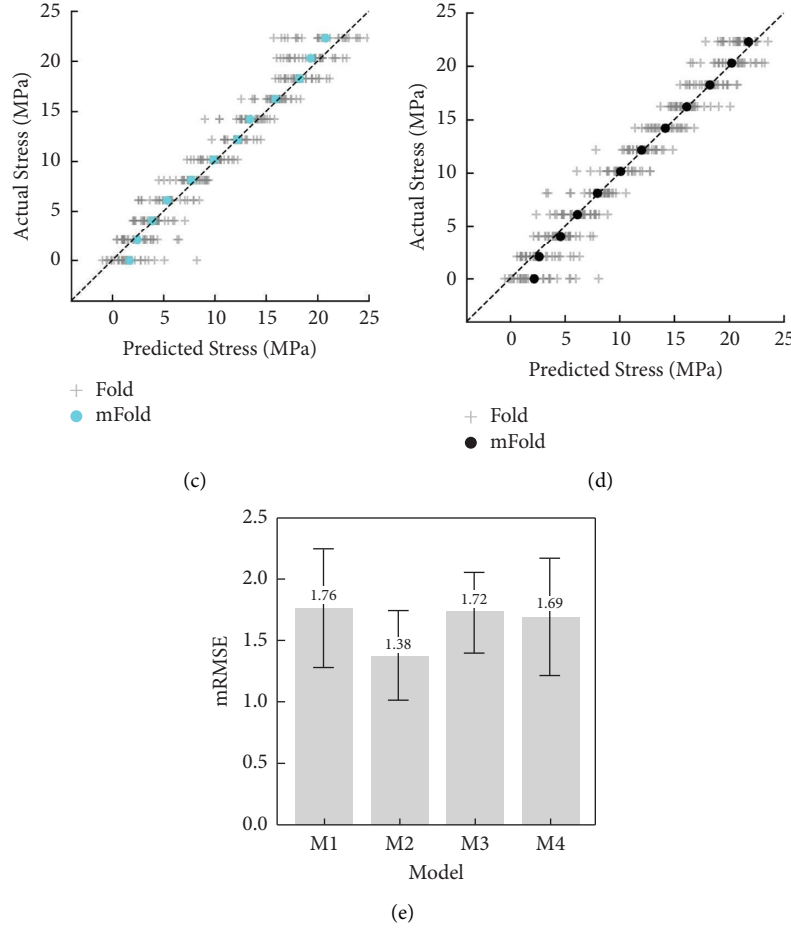


FIGURE 28: The evaluation results of the four 1D CNN architectures (M1–M4). (a) M1. (b) M2. (c) M3. (d) M4. (e) Comparison of mRMSE.

levels, even when trained with limited EMI signals corresponding to a few stress levels.

5. Conclusion

This study aimed to develop the stress monitoring method via smart aggregate (SA)-based EMI monitoring integrated with the 1D CNN deep learning. The EMI measurement model was designed for the SA-embedded concrete body under compression. The 1D CNN model was developed for deep learning raw EMI signals corresponding to various stress levels. Three approaches for concrete stress monitoring were designed to deal with data availability, signal noises, and untrained stress levels. The compressive experiments were conducted on three SA-embedded concrete cylinders to build databanks for the 1D CNN model. The performance of the proposed stress-monitoring method was extensively evaluated for the SA-embedded concrete cylinders to investigate the feasibility of the K-fold cross-validation to deal with the data availability and the effects of noises and untrained data on the accuracy of stress estimation.

Based on the analyzed results, the following conclusions could be drawn:

- (1) The proposed 1D CNN model successfully extracted hidden damage features from raw EMI signals obtained

from SA sensors. The model was implemented to autonomously process these signals and accurately estimate concrete stress values in units of MPa;

- (2) The proposed model accurately estimated the stress values in the three concrete cylinders across twelve stress levels. In the 10-fold cross-validation, the stress prediction exhibited good performance, with RMSE errors ranging from 0.85 to 2.14 MPa. On average, the stress prediction results were closely aligned with the actual stress values, except for the stress level S_1 . It suggests that the K-fold cross-validation has the feasibility to deal with the data availability issue due to real-world EMI measurement.
- (3) The accuracy of the 1D CNN model was noticeably affected by the addition of noise to the EMI signals. The RMSE errors in stress prediction exhibited a linear increase as the percentage of noise was increased. The effect of the noise level on the model accuracy could be adjusted by employing empirical functions. These functions allow for calibration and optimization to mitigate the adverse effects of noise on the performance of the 1D CNN model.
- (4) The accuracy of the 1D CNN model was quite decreased as many stress levels were excluded from the

training datasets. It is observed that the model possesses a certain level of generalization ability and can effectively extrapolate to unseen stress levels based on the limited training data it received. The 1D CNN model was capable of accurately predicting most stress levels with partially untrained databank and, therefore, is promising for realistic applications.

Despite those promising outcomes of the proposed methodology, some further researches still remain. (1) When an internal crack is occurred in concrete specimens, the change in the EMI signatures can be induced by not only the applied stress but also the crack damage. Therefore, the architecture of the proposed 1D CNN model should be improved to not only predict the stress value but also differentiate the stress effect and the damage effect. (2) The adaptability of the methodology will be further researched for practical applications with different stress types and concrete mixture proportions. Transfer learning techniques should be implemented to effectively retrain the 1D CNN model for new applications [65]. Since the 1D CNN model was already well-trained by compressive stress data, it can be conveniently retrained to predict other stress types or to deal with other concrete types with only limited data. (3) The hyperparameters and the kernel size of the 1D CNN model should be fine-tuned using an optimization method to better predict concrete stress in the test specimens.

Appendix

A. Comparison of 1D CNN Architectures

A preliminary study was conducted to select an appropriate 1D CNN architecture for concrete stress monitoring. Four 1D CNN architectures (M1–M4) were designed based on the previous well-established 1D CNN model [47]. Then, the performance of the four architectures was compared using the 10-fold cross-validation method (see Section 2.4) using the configuration of databank (see Section 4.1.1).

The specifications of M1–M4 are depicted in Table 5. While the input and output of these architectures are identical, their depth is different. The architecture M1 was constructed with three Conv layers, as presented in Table 5. The ReLu and Maxpool layers orderly follow the convolutional layers. Three Fc layers follow the final Maxpool layer. The architectures M2–M4 were built by increasing the depth of M1. Specifically, a set of three sequential layers of M1, which are layer 7 (Conv), layer 8 (ReLu), and layer 9 (Maxpool), was doubled, tripled, and quadrupled to create M2, M3, and M4, respectively. Further details regarding the depth, filters, and strides of each layer in M1–M4 are described in Table 5.

The performance of M1–M4 was trained and evaluated using the training and evaluation fold datasets for 10 folds (see Section 4.1.1). Figure 27 shows the training loss value of the four architectures during the learning procedure of 100 epochs. The loss values were plotted in mean with a confidence interval of standard deviation of the 10 training folds. As seen in the figure, the loss values quickly dropped after

the first forty epochs and gradually decreased until the last iteration. All architectures were well-converged after the learning process. It is observed that the learning efficiency of M3 and M4 were lower than M2 and M1 although they were built in more depth. Among the four architectures, M2 exhibited the lowest loss value in the learning process, followed by M1, M4, M3. The M2 architecture was effectively trained in 100 epochs, outperforming the other architectures in terms of learning optimal damage features from EMI datasets.

Figure 28 shows the stress prediction results of M1–M4 when tested using 10 evaluation folds. In Figures 28(a)–28(d), the legend “Fold” signifies the predicted stress results for 10-folds, which are cumulatively plotted. The mean of the predicted stress values is denoted by the legend “mFold”. It is observed that the predicted stress points are varied around the mean. The prediction results of the four architectures are quite accurate with similar patterns. However, it is found that the M2 architecture showed a better performance than others in predicting a higher stress above 10 MPa. Figure 28 compares the mean values of the testing RMSE (mRMSE) of the architectures M1–M4, with the error bars signifying standard deviation of RMSE values derived from 10-folds. Among the four architectures, M2 exhibited the lowest mRMSE value (1.38 MPa), followed by M4 (1.69 MPa), M3 (1.72 MPa), and M1 (1.76 MPa). The standard deviation of M3 is the lowest, followed by M2, M4, and M1. Despite that the standard deviation of M2 is slightly higher than M3, its mRMSE value is considerably lower than that of M3. Therefore, the M2 architecture was selected for the 1D CNN-based concrete stress prediction model.

Data Availability

The data used to support the findings of this study are available from the corresponding author upon request.

Conflicts of Interest

The authors declare that they have no conflicts of interest.

Acknowledgments

This work was supported by the Basic Science Research Program through the National Research Foundation of Korea (2022R1A2C10038891161782064340101).

References

- [1] M. K. I. Khan, C. K. Lee, Y. X. Zhang, and M. M. Rana, “Compressive behaviour of ECC confined concrete partially encased steel composite columns using high strength steel,” *Construction and Building Materials*, vol. 265, Article ID 120783, 2020.
- [2] A. Smolana, B. Klemczak, M. Azenha, and D. Schlicke, “Experiences and analysis of the construction process of mass foundation slabs aimed at reducing the risk of early age cracks,” *Journal of Building Engineering*, vol. 44, Article ID 102947, 2021.
- [3] T. U. Kim, H. V. Le, J. W. Park, S. K. Eock, Y. Jang, and D. J. Kim, “Development of a smart concrete block with an

- eccentric load sensing capacity,” *Construction and Building Materials*, vol. 306, Article ID 124881, 2021.
- [4] T. Suzuki, T. Shiotani, and M. Ohtsu, “Evaluation of cracking damage in freeze-thawed concrete using acoustic emission and X-ray CT image,” *Construction and Building Materials*, vol. 136, pp. 619–626, 2017.
 - [5] E. Bayraktar, S. D. Antolovich, and C. Bathias, “New developments in non-destructive controls of the composite materials and applications in manufacturing engineering,” *Journal of Materials Processing Technology*, vol. 206, no. 1–3, pp. 30–44, 2008.
 - [6] X. Tan, A. Abu-Obeidah, Y. Bao, H. Nassif, and W. Nasreddine, “Measurement and visualization of strains and cracks in CFRP post-tensioned fiber reinforced concrete beams using distributed fiber optic sensors,” *Automation in Construction*, vol. 124, Article ID 103604, 2021.
 - [7] Q. Q. Pham, N. L. Dang, and J. T. Kim, “Piezoelectric sensor-embedded smart rock for damage monitoring in a prestressed anchorage zone,” *Sensors*, vol. 21, no. 2, p. 353, 2021.
 - [8] S. J. Lee, D. Ahn, I. You, D. Y. Yoo, and Y. S. Kang, “Wireless cement-based sensor for self-monitoring of railway concrete infrastructures,” *Automation in Construction*, vol. 119, Article ID 103323, 2020.
 - [9] L. Sun, Q. Ma, F. Han et al., “Experimental investigation on axial compression behavior of steel reinforced concrete columns with welded stirrups,” *Engineering Structures*, vol. 208, Article ID 109924, 2020.
 - [10] S. A. Neild, M. S. Williams, and P. D. Mcfadden, “Development of a vibrating wire strain gauge for measuring small strains in concrete beams,” *Strain*, vol. 41, no. 1, pp. 3–9, 2005.
 - [11] X. Zhao, F. Wen, T. M. Chan, and S. Cao, “Theoretical stress-strain model for concrete in steel-reinforced concrete columns,” *Journal of Structural Engineering*, vol. 145, no. 4, Article ID 04019009, 2019.
 - [12] H. P. Wang, J. G. Dai, and X. Z. Wang, “Improved temperature compensation of fiber Bragg grating-based sensors applied to structures under different loading conditions,” *Optical Fiber Technology*, vol. 63, Article ID 102506, 2021.
 - [13] W. S. Na and J. Baek, “A review of the piezoelectric electromechanical impedance based structural health monitoring technique for engineering structures,” *Sensors*, vol. 18, no. 5, p. 1307, 2018.
 - [14] C. Liang, F. P. Sun, and C. A. Rogers, “Coupled electro-mechanical analysis of adaptive material systems-determination of the actuator power consumption and system energy transfer,” *Journal of Intelligent Material Systems and Structures*, vol. 5, no. 1, pp. 12–20, 1994.
 - [15] C. K. Soh, K. K. Tseng, S. Bhalla, and A. Gupta, “Performance of smart piezoceramic patches in health monitoring of a RC bridge,” *Smart Materials and Structures*, vol. 9, no. 4, pp. 533–542, 2000.
 - [16] G. Song, H. Gu, and Y. L. Mo, “Smart aggregates: multi-functional sensors for concrete structures- a tutorial and a review,” *Smart Materials and Structures*, vol. 17, no. 3, Article ID 033001, 2008.
 - [17] Q. Q. Pham, N. L. Dang, Q. B. Ta, and J. T. Kim, “Optimal localization of smart aggregate sensor for concrete damage monitoring in PSC anchorage zone,” *Sensors*, vol. 21, no. 19, p. 6337, 2021.
 - [18] T.-C. Huynh, N.-L. Dang, and J.-T. Kim, “Advances and Challenges in impedance-based structural health monitoring,” *Structural Monitoring and Maintenance*, vol. 4, pp. 301–329, 2017.
 - [19] Q.-Q. Pham, Q.-B. Ta, J.-H. Park, and J.-T. Kim, “Raspberry Pi platform wireless sensor node for low-frequency impedance responses of PZT interface,” *Sensors*, vol. 22, no. 24, p. 9592, 2022.
 - [20] J. T. Kim, K. D. Nguyen, and T. C. Huynh, “Wireless health monitoring of stay cable using piezoelectric strain response and smart skin technique,” *Smart Structures and Systems*, vol. 12, no. 3_4, pp. 381–397, 2013.
 - [21] T. C. Huynh and J. T. Kim, “FOS-Based prestress force monitoring and temperature effect estimation in unbonded tendons of PSC girders,” *Journal of Aerospace Engineering*, vol. 30, no. 2, pp. 1–14, 2017.
 - [22] T. C. Huynh, S. Y. Lee, N. L. Dang, and J.-T. Kim, “Sensing region characteristics of smart piezoelectric interface for damage monitoring in plate-like structures,” *Sensors*, vol. 19, no. 6, p. 1377, 2019.
 - [23] W. Chung and D. Kang, “Full-scale test of a concrete box girder using FBG sensing system,” *Engineering Structures*, vol. 30, no. 3, pp. 643–652, 2008.
 - [24] T.-C. Huynh and J.-T. Kim, “Quantitative damage identification in tendon anchorage via PZT interface-based impedance monitoring technique,” *Smart Structures and Systems*, vol. 20, no. 2, pp. 181–195, 2017.
 - [25] T. C. Huynh and J. T. Kim, “RBFN-based temperature compensation method for impedance monitoring in prestressed tendon anchorage,” *Structural Control and Health Monitoring*, vol. 25, no. 6, Article ID e2173, 2018.
 - [26] F. P. Sun, Z. Chaudhry, C. Liang, and C. A. Rogers, “Truss structure integrity identification using PZT sensor-actuator,” *Journal of Intelligent Material Systems and Structures*, vol. 6, no. 1, pp. 134–139, 1995.
 - [27] A. N. Zagrai and V. Giurgiutiu, “Electro-mechanical impedance method for crack detection in thin plates,” *Journal of Intelligent Material Systems and Structures*, vol. 12, no. 10, pp. 709–718, 2001.
 - [28] J. Min, S. H. Park, and C. B. Yun, “Impedance-based structural health monitoring using neural networks for autonomous frequency range selection,” *Smart Materials and Structures*, vol. 19, no. 12, Article ID 125011, 2010.
 - [29] G. Park, H. Sohn, C. R. Farrar, and D. J. Inman, “Overview of piezoelectric impedance-based health monitoring and path forward,” *The Shock and Vibration Digest*, vol. 35, no. 6, pp. 451–463, 2003.
 - [30] F. G. Yuan, S. A. Zargar, Q. Chen, and S. Wang, “Machine learning for structural health monitoring: challenges and opportunities,” *Sensors and smart structures technologies for civil, mechanical, aerospace systems*, vol. 11379, 2020.
 - [31] O. Abdeljaber, O. Avci, M. S. Kiranyaz, B. Boashash, H. Sodano, and D. J. Inman, “1-D CNNs for structural damage detection: verification on a structural health monitoring benchmark data,” *Neurocomputing*, vol. 275, pp. 1308–1317, 2018.
 - [32] W. S. Na, “A portable bolt-loosening detection system with piezoelectric-based nondestructive method and artificial neural networks,” *Structural Health Monitoring*, vol. 21, no. 2, pp. 683–694, 2021.
 - [33] M. A. De Oliveira, A. V. Monteiro, and J. Vieira Filho, “A new structural health monitoring strategy based on PZT sensors and convolutional neural network,” *Sensors*, vol. 18, no. 9, p. 2955, 2018.
 - [34] T. T. Nguyen, J. T. Kim, Q. B. Ta, D. D. Ho, T. T. V. Phan, and T. C. Huynh, “Deep learning-based functional assessment of piezoelectric-based smart interface under various

- degradations,” *Smart Structures and Systems*, vol. 28, no. 1, pp. 69–87, 2021.
- [35] T. T. Nguyen, T. Tuong Vy Phan, D. D. Ho, A. Man Singh Pradhan, and T. C. Huynh, “Deep learning-based autonomous damage-sensitive feature extraction for impedance-based prestress monitoring,” *Engineering Structures*, vol. 259, Article ID 114172, 2022.
 - [36] T. C. Huynh, J. H. Park, H. J. Jung, and J. T. Kim, “Quasi-autonomous bolt-loosening detection method using vision-based deep learning and image processing,” *Automation in Construction*, vol. 105, Article ID 102844, 2019.
 - [37] T.-T. Nguyen, Q.-B. Ta, D.-D. Ho, J.-T. Kim, and T.-C. Huynh, “A method for automated bolt-loosening monitoring and assessment using impedance technique and deep learning,” *Developments in the Built Environment*, vol. 14, Article ID 100122, 2023.
 - [38] D. Ai, F. Mo, Y. Han, and J. Wen, “Automated identification of compressive stress and damage in concrete specimen using convolutional neural network learned electromechanical admittance,” *Engineering Structures*, vol. 259, Article ID 114176, 2022.
 - [39] D. Ai and J. Cheng, “A deep learning approach for electromechanical impedance based concrete structural damage quantification using two-dimensional convolutional neural network,” *Mechanical Systems and Signal Processing*, vol. 183, Article ID 109634, 2023.
 - [40] D. Ai, F. Mo, J. Cheng, and L. Du, “Deep learning of electromechanical impedance for concrete structural damage identification using 1-D convolutional neural networks,” *Construction and Building Materials*, vol. 385, Article ID 131423, 2023.
 - [41] Y. Yu, S. Liang, B. Samali et al., “Torsional capacity evaluation of RC beams using an improved bird swarm algorithm optimised 2D convolutional neural network,” *Engineering Structures*, vol. 273, Article ID 115066, 2022.
 - [42] Q. Yan, X. Liao, C. Zhang, Y. Zhang, S. Luo, and D. Zhang, “Intelligent monitoring and assessment on early-age hydration and setting of cement mortar through an EMI-integrated neural network,” *Measurement*, vol. 203, Article ID 111984, 2022.
 - [43] C. Zhang, Q. Yan, Y. Zhang, X. Liao, and H. Zhong, “Intelligent monitoring of concrete-rock interface debonding via ultrasonic measurement integrated with convolutional neural network,” *Construction and Building Materials*, vol. 400, Article ID 131865, 2023.
 - [44] G. Li, M. Luo, J. Huang, and W. Li, “Early-age concrete strength monitoring using smart aggregate based on electromechanical impedance and machine learning,” *Mechanical Systems and Signal Processing*, vol. 186, Article ID 109865, 2023.
 - [45] O. Abdeljaber, O. Avci, S. Kiranyaz, M. Gabbouj, and D. J. Inman, “Real-time vibration-based structural damage detection using one-dimensional convolutional neural networks,” *Journal of Sound and Vibration*, vol. 388, pp. 154–170, 2017.
 - [46] T. C. Huynh, T. D. Nguyen, D. D. Ho, N. L. Dang, and J. T. Kim, “Sensor fault diagnosis for impedance monitoring using a piezoelectric-based smart interface technique,” *Sensors*, vol. 20, no. 2, p. 510, 2020.
 - [47] U. R. Acharya, H. Fujita, S. L. Oh, Y. Hagiwara, J. H. Tan, and M. Adam, “Application of deep convolutional neural network for automated detection of myocardial infarction using ECG signals,” *Information Sciences*, vol. 415, pp. 190–198, 2017.
 - [48] Y. Zhang and B. Wallace, “A sensitivity analysis of (and practitioners’ guide to) convolutional neural networks for sentence classification,” 2015, <https://arxiv.org/abs/1510.03820>.
 - [49] S. Tyagi and S. Mittal, “Sampling approaches for imbalanced data classification problem in machine learning,” *Proceedings of ICRIC 2019: Recent Innovations in Computing*, Springer International Publishing, Berlin, Germany, pp. 209–221, 2020.
 - [50] StratifiedShuffleSplit, “Stratified shuffle split,” 2022, https://scikit-learn.org/stable/modules/generated/sklearn.model_selection.StratifiedShuffleSplit.html.
 - [51] A. Jalloh, *Effects of Piezoelectric (PZT) Sensor Bonding and the Characteristics of the Host Structure on Impedance Based Structural Health Monitoring*, Nasa Faculty Fellowship Program, Mechanical Engineering Department Alabama A&M University, Normal, AL 35762, USA, 2005.
 - [52] C. W. Helstrom, “The resolution of signals in white, Gaussian noise,” *Proceedings of the IRE*, vol. 43, no. 9, pp. 1111–1118, 1955.
 - [53] J. Melville, K. S. Alguri, C. Deemer, and J. B. Harley, “Structural damage detection using deep learning of ultrasonic guided waves,” *AIP Conference Proceedings*, vol. 1949, no. 1, Article ID 230004, 2018.
 - [54] A. Kocherla and K. V. Subramaniam, “Embedded smart PZT-based sensor for internal damage detection in concrete under applied compression,” *Measurement*, vol. 163, Article ID 108018, 2020.
 - [55] J. G. Macgregor, J. K. Wight, S. Teng, and P. Irawan, *Reinforced concrete: Mechanics and Design*, Prentice Hall, Upper Saddle River, NJ, USA, 1997.
 - [56] T. J. Saravanan, K. Balamonica, C. B. Priya, A. L. Reddy, and N. Gopalakrishnan, “Comparative performance of various smart aggregates during strength gain and damage states of concrete,” *Smart Materials and Structures*, vol. 24, no. 8, Article ID 085016, 2015.
 - [57] E. G. Nawy, *Prestressed concrete. A Fundamental Approach*, Prentice Hall, Upper Saddle River, New Jersey, 1996.
 - [58] D. Ai, C. Lin, and H. Zhu, “Embedded piezoelectric transducers based early-age hydration monitoring of cement concrete added with accelerator/retarder admixtures,” *Journal of Intelligent Material Systems and Structures*, vol. 32, no. 8, pp. 847–866, 2020.
 - [59] T. C. Huynh and J. T. Kim, “Impedance-based cable force monitoring in tendon-anchorage using portable PZT-interface technique,” *Mathematical Problems in Engineering*, vol. 2014, pp. 1–11, 2014.
 - [60] <https://www.python.org/>, 2022.
 - [61] D. P. Kingma and J. Ba, “Adam: a method for stochastic optimization,” 2014, <https://arxiv.org/abs/1412.6980>.
 - [62] L. M. Campeiro, D. E. Budoya, and F. G. Baptista, “Damage detection in noisy environments based on EMI and Lamb waves: a comparative study,” *Journal of Intelligent Material Systems and Structures*, vol. 34, no. 9, pp. 1042–1056, 2023.
 - [63] B. A. De Castro, F. G. Baptista, and F. Ciampa, “Comparative analysis of signal processing techniques for impedance-based SHM applications in noisy environments,” *Mechanical Systems and Signal Processing*, vol. 126, pp. 326–340, 2019.
 - [64] B. A. De Castro, F. G. Baptista, and F. Ciampa, “New imaging algorithm for material damage localisation based on impedance measurements under noise influence,” *Measurement*, vol. 163, Article ID 107953, 2020.
 - [65] K. Weiss, T. M. Khoshgoftaar, and D. Wang, “A survey of transfer learning,” *Journal of Big Data*, vol. 3, no. 1, pp. 9–40, 2016.